

Morphologies and stellar populations of galaxies in the core of Abell 2218

S.F.Sánchez, N.Cardiel^{2,1}, M.A.W.Verheijen³, S.Pedraz^{1,2} and G.Covone⁴

¹*Centro Astronómico Hispano Alemán, Calar Alto, (CSIC-MPI), C/Jesús Durbán Remón 2-2, 04004-Almería, Spain*

²*Departamento de Astrofísica, Facultad de Físicas, Universidad Complutense de Madrid, 28040 Madrid, Spain*

³*Kapteyn Astronomical Institute, PO Box 800, 9700 AV Groningen, The Netherlands*

⁴*INAF-Osservatorio Astronomico di Capodimonte, Naples, Italy*

To be edited later (March 2006)

ABSTRACT

We present a study of the stellar populations and morphologies of galaxies in the core of the galaxy cluster Abell 2218. Integral field spectroscopy (IFS) observations were performed using PMAS in the PPAK mode covering a field-of-view of $\sim 74'' \times 64''$ centred on the core of the cluster, in order to obtain spectroscopy of an unbiased flux limited sample of cluster galaxies. Forty-three objects were detected in the IFS data, 31 of them with enough signal-to-noise to derive the redshift, all of them brighter than $I < 21.5$ mag. Twenty-eight are at the redshift of the cluster (17 with previously unknown redshift). Individual spectra of the cluster members were extracted and compared with single stellar population models to derive the luminosity-weighted ages and metallicities. In addition, deep HST/ACS F475W, F555W, F625W and F850LP-band images centred on the cluster core were obtained from the HST archive ($z_{\text{lim}} \sim 28$ mag). A detailed morphological analysis of all the galaxies within the field-of-view of these images down to $z_{\text{lim}} < 22.5$ mag was performed classifying them as late-type, intermediate and early-type, on the basis of their Sérsic indices. The literature was scanned to look for spectroscopically confirmed cluster members located within the field-of-view of the ACS image. The final sample of 59 galaxies comprises our reported sample of 28 galaxies in the core, and 31 additional galaxies in the outer regions. In addition, multiband broad-band photometry was extracted from the literature for all objects.

The morphologically segregated color-magnitude diagram shows that the early-type galaxies cover the range of brighter and redder colors (the so-called “red sequence”). A large fraction of spiral galaxies ($\sim 50\%$) is found, most of them fainter than the limit of previous studies. They cover a wide range in colors, from blue colors typical of Butcher-Oemler galaxies to red colors similar to those of early-type galaxies. This result indicates that early-type galaxies are more massive and have older stellar populations, while late-type galaxies are less massive and have a wider range of stellar populations. The distribution of luminosity weighted ages as a function of metallicities and luminosity weighted masses, and the distribution of Sérsic indices as a function of the luminosity weighted masses confirm these results. They in fact agree with a proposed two-step scenario for the evolution of galaxies in clusters, where the star formation is quenched first in the infalling spirals, after which a morphological transformation follows that requires larger time-scales. This scenario naturally explains the population faint late-type galaxies with old stellar populations observed in this cluster. In addition, an extremely blue merging galaxy system is found at the core, with the nominal redshift of the cluster.

Key words: galaxies: clusters: individual: Abell 2218 - galaxies: elliptical and lenticular, cD - galaxies: spiral - galaxies: irregular - galaxies: fundamental parameters - galaxies: stellar content - techniques: spectroscopic

arXiv:astro-ph/0611660v2 22 Nov 2006

1 INTRODUCTION

Galaxy clusters have been used for decades to study the evolution of galaxies. Being tracers of the largest density enhancements in the Universe, they are considered the regions where galaxies formed first. At low redshift they are dominated by large early-type galaxies (E/S0), which colors are consistent with a bulk formation of their stars at high redshift. Classically, it was thought that the evolution of this dominant population through different cosmological epochs was largely passive without signatures of important deviations (ie., periods of more recent star formation). However, this simple picture has changed in the last decades. Butcher et al. (1983) and Butcher & Oemler (1984) showed an increase in the fraction of blue galaxies in clusters with redshift. High-resolution ground-based and HST images have shown that they correspond to galaxies with late-type morphologies, often disturbed or with close companions (e.g. Thompson 1986, 1988; Couch et al. 1994; Dressler et al. 1994, 1997). One observes a morphological evolution of the galaxies in clusters, in the sense that the fraction of E-type galaxies remains constant as a function of different cosmological epochs, while the fraction of S0's increases at the expense of L-types towards lower redshift (e.g. Fasano et al. 2000).

The presence in clusters of a significant population of post-starburst galaxies known as “E+A” or “k+a” galaxies (Dressler & Gunn 1983; Couch & Sharples 1987), indicates that star formation was active in the recent past and sharply halted at some point during the last 1-1.5 Gyr (Poggianti 2003, 2004). Most of these galaxies are late type, and they show a radial distribution within the clusters that is intermediate between the passive and the emission-line galaxy populations (Poggianti et al. 1999). These results lead to the hypothesis of a two-step evolution of galaxies. A spiral galaxy is captured by the cluster and, during its infall, suffers from gas-stripping due to the tidal forces involved (e.g. Verheijen 1997). Provoked by the lack of gas, the star formation is halted, and the galaxy evolves passively, being observed as a “k+a” post-starburst. An initial short starburst process, previous to the gas-stripping, may be also present (Poggianti 2004). After this the galaxy evolves morphologically over larger times scales. The disk dims due to the lack of a new generation of stars, that otherwise will dominate its luminosity, and the galaxy transforms itself into a lenticular galaxy. Dry mergers between lenticular and spheroidal galaxies build up new large spheroidals (e.g. Bell et al. 2006)

The proposed scenario suggests that a fraction of the observed S0's were previously star-forming spirals. For these galaxies the star formation was truncated at some time between 2 and 5 Gyr ago and it is expected that their luminosity faded by ~ 0.5 – 1.5 mag and become redder (Poggianti et al. 2001), populating the red sequence at magnitudes fainter than the brightest 1 or 2 magnitudes (Poggianti 2003). The same process may affect dwarf galaxies captured by the cluster, which will suffer more strongly the effects of tidal interaction and galaxy harassment, which induces a short but intense starburst (Moore et al. 1996; Rakos et al. 2001). Most of the field dwarf galaxies are gas-rich rich, blue galaxies with late-type morphologies at any redshift (Cairós et al. 2001; Barazza et al. 2006). Once captured by the cluster, consumed or stripped of its gas, it is

Table 1. Summary of the HST/ACS images

Filter	Pivot λ Å	Width Å	Number Frames	Exp.time seconds	mag_{lim} (15σ)
F475W	4744.356	418.80	3	4267.0	27.42
F555W	5359.547	375.19	4	5601.0	28.04
F625W	6310.454	415.31	5	7013.0	28.08
F775W	7693.026	432.03	8	10732.0	27.46
F850LP	9054.768	538.95	12	11776.0	28.22

expected that their luminosity fades and they become redder too, populating the faint-end of the red sequence. In both cases one expects to find a population of red late-type galaxies, fainter than the original early-type galaxies in the cluster. However, most of the previous studies have found that late-type galaxies are mostly blue (e.g. Thompson 1986).

To test this hypothesis, complete spectroscopic surveys of cluster galaxies and high-resolution deep images for a proper morphological analysis of the faintest possible targets are required. Complete spectroscopic surveys are difficult and time consuming, due to the requirement of deblending and placing objects in the spectrograph multislits or masks. In particular, the blending of different components in the core of the clusters is a problem, impossible to handle with classical slit spectroscopy. Due to that, most of the spectroscopic surveys are based on pre-selection of the cluster candidates, most of them based on color or morphological selections (e.g. Dressler et al. 1999; Balogh et al. 1999; Kelson et al. 2000; Ziegler et al. 2001; Fritz et al. 2005). Alternatively, they are focused on galaxies in the less crowded outer regions. These selections may affect substantially the conclusions. For these reasons we have started an observational program aimed at obtaining Integral Field Spectroscopy (IFS) of the core of some of the richest galaxy clusters in the local universe, including Abell 1689 (ESO 73.A-0605) and Abell 2218. For both of them deep HST/ACS images are available. A similar approach has been used before by Covone et al. (2006), to study the dynamical mass of low redshift galaxy clusters.

Abell 2218 is one of the richest clusters in the Abell catalogue (Abell et al. 1989), with a richness class of 4. It has a redshift of $z \sim 0.17$, and a velocity dispersion of 1370 km s^{-1} (Kristian et al. 1978; Le Borgne et al. 1992). The cluster shows a set of arc-lenses. Detailed high-resolution X-ray maps (McHardy et al. 1990) and mass-concentration studies based on the properties of the gravitational lenses have shown that the cluster has two density peaks, the strongest of them dominated by a large cD galaxy. Several observational programs have provided us with a large dataset of well deblended slit spectra for the galaxies in the outer part of the cluster (Ziegler et al. 2001), as well as very good multiband ground-based and HST imaging (Le Borgne et al. 1992; Smail et al. 2001; Ziegler et al. 2001). We focused our survey on the central arcmin region of the cluster, around the cD galaxy.

The outline of this article is as follows. Section 2 describes the observational dataset, including a description of the IFS data and the HST/ACS images. Section 3 includes the analysis of the dataset and presents the results. Here, Sections 3.1 and 3.2 describe the automatic morphological

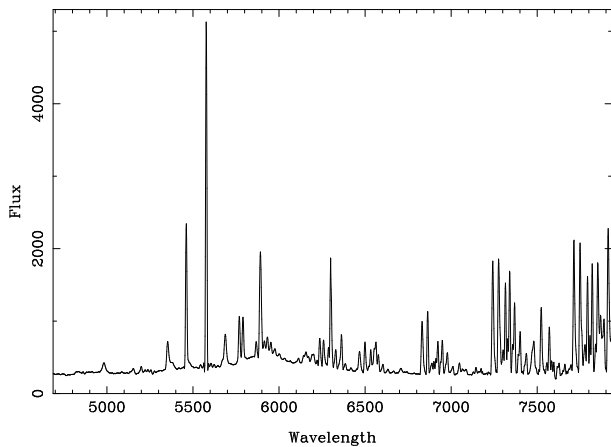


Figure 1. Average night-sky emission spectrum derived by combining the spectra obtained through the 36 sky-fibers for the different pointings of each night.

analysis that we performed as opposed to classical methods. Section 3.3 shows the method used to deblend and extract the integrated spectra of the different detected objects from the IFS data, with the redshift determination explained in Section 3.4. The analysis of the morphologically segregated color-magnitude diagram is included in Section 3.5. The luminosity weighted ages and metallicities of the galaxies, and their relation to their masses and morphologies are discussed in Section 3.6 and 3.7. The results are discussed in Section 4, and the conclusions are listed in Section 5. Throughout this article we have used a Λ -cosmology, with $H_0=70 \text{ km s}^{-1} \text{ Mpc}^{-1}$, $\Omega_m=0.3$ and $\Omega_\Lambda=0.7$.

2 OBSERVATIONAL DATASET

2.1 IFS observations and data reduction

Observations were carried out on June the 30th and July the 6th, 2005, at the 3.5m telescope at Calar Alto Observatory with the Potsdam MultiAperture Spectrograph, PMAS, (Roth et al. 2005) in the PPAK mode (Verheijen et al. 2004; Kelz et al. 2006). The V300 grating was used, covering a wavelength range between 4650–8000 Å with a resolution of $\sim 10 \text{ Å FWHM}$ and a sampling of 3.2 Å/pixel . The PPAK fiber bundle consists of 382 fibers of $2.7''$ diameter each one. Of them, 331 fibers (the science fibers) are concentrated in a single hexagonal bundle covering a field-of-view of $72'' \times 64''$, with a filling factor of $\sim 65\%$. The sky is sampled by 36 additional fibers, distributed in 6 bundles of 6 fibers each one, located following a circular distribution at $\sim 90''$ from the center and at the edges of the central hexagon. The sky-fibers are distributed between the science ones in a pseudo-slit, in order to have a good characterization of the sky. The remaining 15 fibers are used for calibration purposes, as described below.

For each night, three dithered exposures of 1 hour each were taken, following a pattern of $\Delta RA = +1.56''$ and $\Delta DEC = \pm 0.78''$, in order to have a complete coverage of the science field-of-view and to increase the spatial resolution. Each pointing was divided into shorter individual frames for a proper cosmic-ray removal. A total of 6 hours integration

time was achieved after combining the exposures of the two nights (3 hours per night).

Data reduction was performed using R3D (Sánchez & Cardiel 2005; Sánchez 2006), in combination with the IRAF package (Tody 1993)¹ and E3D (Sánchez et al. 2004a). The reduction consists of the standard steps for fiber-based integral-field spectroscopy. A master bias frame was created by averaging all the bias frames observed during the night and subtracted from the science frames. The location of the spectra in the CCD was determined using a continuum illuminated exposure taken before the science exposures. Each spectrum was extracted from the science frames by coadding the flux in 5 pixels in the perpendicular direction of each fiber, and stored in a row-staked-spectrum file RSS (Sánchez et al. 2004a). Wavelength calibration was performed using a He lamp exposure taken at the beginning of the night, and corrected for distortions using ThAr exposures obtained simultaneously with the science exposures through the calibration fibers (indicated above). The final accuracy of the wavelength calibration was estimated by comparing the central wavelength of the sky-emission lines with their nominal values, finding an agreement within a range of $\sim 0.3 \text{ Å}$. Differences in the fiber-to-fiber transmission throughput were corrected for by comparing the wavelength-calibrated RSS science frames with the corresponding continuum illuminated images. Flux calibration was performed using standard calibration stars observed through the night (BD33+2642 and Hz44). The uncalibrated spectra of the stars extracted from the reduced frames were then compared with publically available calibrated spectra, determining a flux calibration correction that was applied to the science frames, once corrected by the differences in exposure time. The accuracy of the spectrophotometric calibration was $\sim 0.15 \text{ mag}$ across the wavelength range covered by our dataset, as determined by comparing with high accurate broad-band photometry, as we will discuss below. A night sky-emission spectrum was obtained for each pointing by combining the 36 spectra obtained through the sky-fibers, and subtracted from the 331 science-fibers spectra. Figure 1 shows the average night-sky spectrum obtained after combining all of them. Several strong night-sky emission lines contaminate our spectra, in particular in the reddest part ($\lambda > 7200 \text{ Å}$).

The three dithered exposures were then combined, creating a single RSS frame with 993 science spectra and the corresponding combination of the position table. A final datacube with $1''/\text{pixel}$ sampling was created for each night by interpolating the combined RSS frame using E3D (Sánchez et al. 2004a). This corresponds to 2.85 kpc/pixel at the redshift of our target. Finally, the two datacubes obtained for each night were recentered at each wavelength, correcting for differential atmospheric refraction, and combined using IRAF tasks. The final datacube comprises 4828 individual spectra, covering a field-of-view of $\sim 71'' \times 68''$.

¹ IRAF is distributed by the National Optical Astronomy Observatories, which are operated by the Association of Universities for Research in Astronomy, Inc., under cooperative agreement with the National Science Foundation.

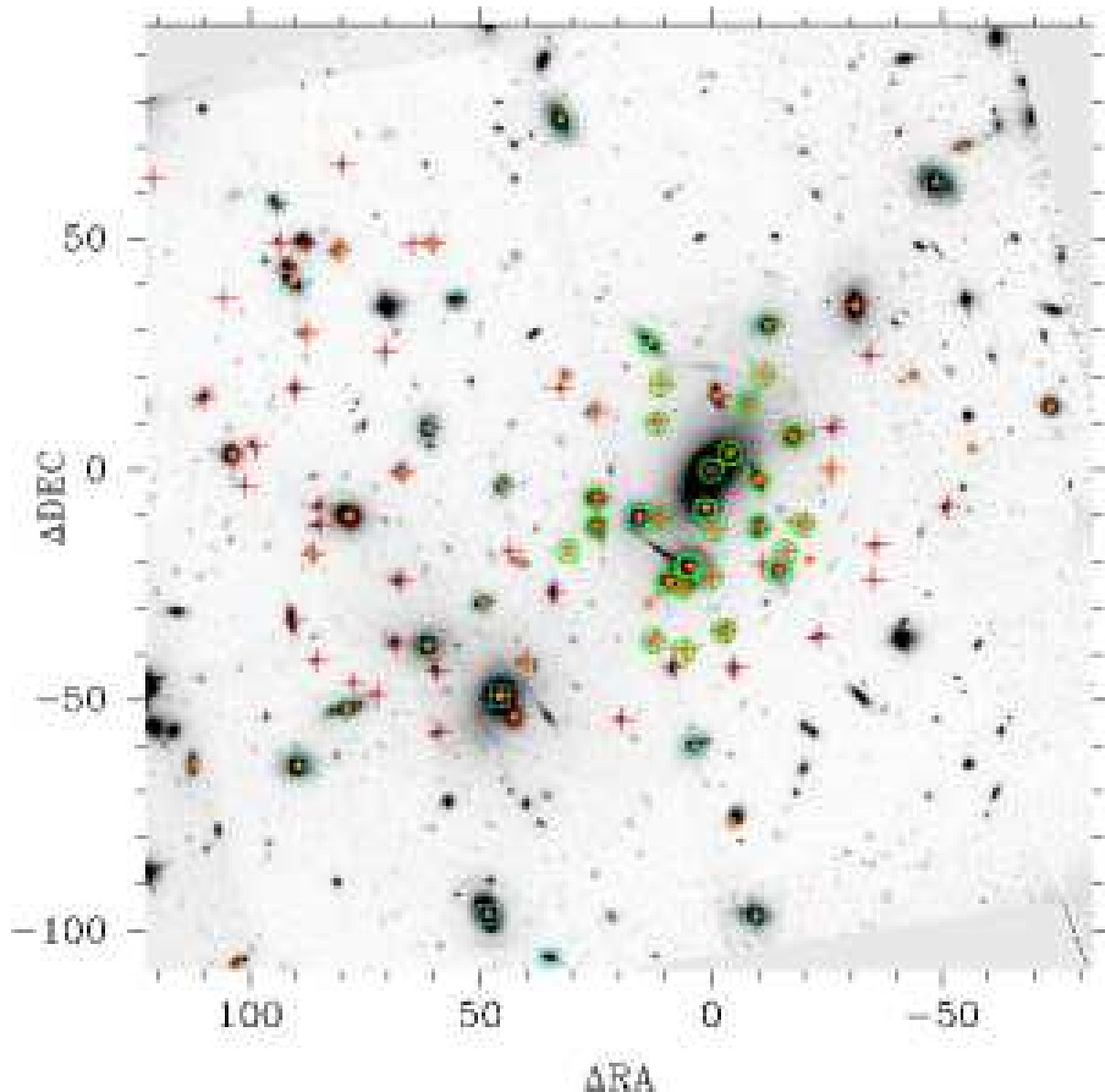


Figure 2. Grayscale image of the combined F850LP-band image, together with labels indicating the location of the galaxies studied by Le Borgne et al. (1992) (orange stars), Ziegler et al. (2001) (blue squares) and Smail et al. (2001) (red crosses). The location of the confirmed cluster members sampled by our IFS data are also indicated (green circles). North is up and East left.

2.2 HST/ACS images and literature data

We obtained publicly available HST/ACS images of the cluster in the F475W, F555W, F625W, F775W and F850LP-bands from the Hubble Space Telescope archive. Table 1 summarizes their main characteristics, including the central wavelength and width of their bands (obtained from Sirianni et al. 2005). They basically correspond to images in the the classical B , V , R , I and z bands. The images were calibrated to the Vega system using the corresponding magnitude zeropoints and prescriptions listed in Sirianni et al. (2005). Table 1 also lists the number of individual frames acquired, each one with a different orientation and a slightly different pointing, due to the observing strategy of the HST/ACS camera (in order to cover the gap in-between the two different CCDs). The acquired frames were already pro-

cessed by the HST/ACS reduction pipeline, which includes bias and dark current correction, flat-fielding, quantum efficiency correction, field-distorsion correction, the derivation of the astrometric-solution and flux calibration. We correct each individual from for cosmic rays, realigned to the standard North-East and finally combined into a single image per filter after a sky-background determination and subtraction. The final exposure time and limiting magnitude of each image, estimated by looking for the faintest object detected at $\sim 15\sigma$ over the background, are listed in Table 1. All the images are much deeper than our IFS data, as we will see below in detail. In particular this is the case for the F850LP-band image. This image is much deeper than the rest, being as deep as the corresponding image of UDF (e.g. Coe et al. 2006), and therefore one of the deepest images ever taken of this cluster. The cluster core is centred on one

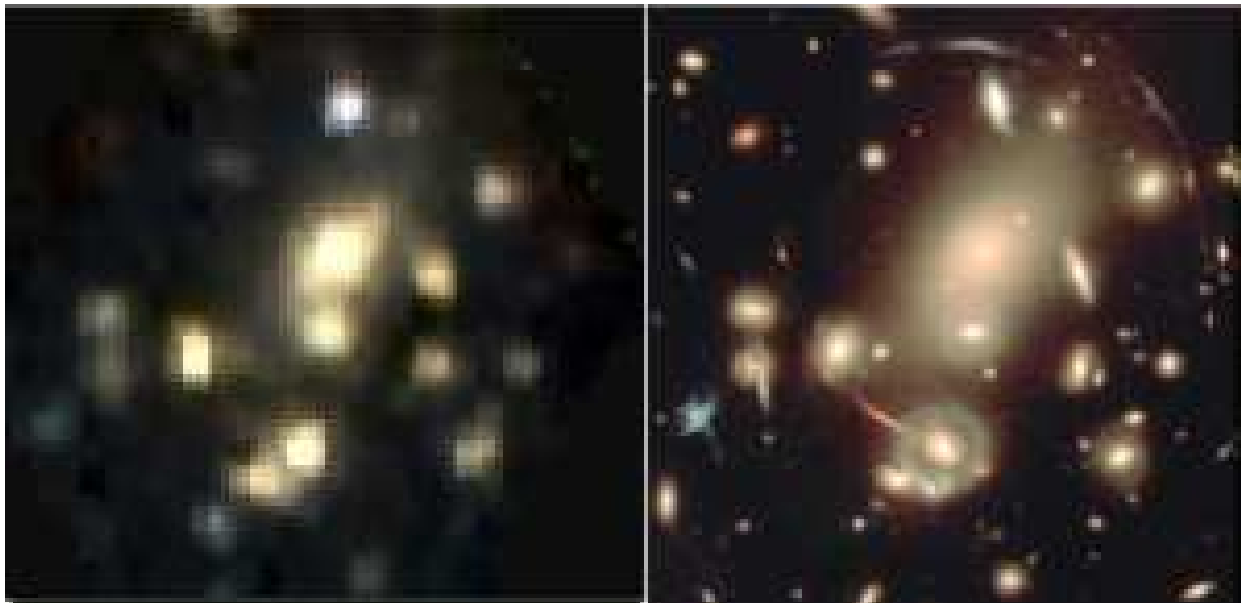


Figure 3. *left-panel:* Three-color image created by coadding the flux of the final datacube through three broad-bands corresponding approximately to B , R and I . *right-panel:* Similar image created using HST/ACS data described in the text. An electronic version of the full size image can be found in the webpage http://www.caha.es/sanchez/abell2218/BRI_big.jpg

of the ACS chips for this particular image, and the field-of-view of our IFS data is completely covered by it. This high resolution ACS F850LP-band image will be used for a detailed morphological analysis.

We also collected broad-band photometry and redshift information of the cluster galaxies available in the literature. Le Borgne et al. (1992) performed a photometric and spectroscopic survey of the galaxies in a field of $4' \times 4'$ centred on Abell 2218. This survey comprises broad-band photometry in 5 bands (B, g, r, i and z filters) for 729 objects, and redshift determination for 66 of them, 51 cluster members. They calibrated their photometric data using two different systems, the Johnson one for the B -band (Johnson & Morgan 1953), and the Thuan-Gunn for the g, r, i and z -band (Thuan & Gunn 1976). We did not perform any recalibration of their data to a common photometric system. These data were initially used to compare with the corresponding intensity of the individual spectra of the objects detected in our IFU data, and for doing so we just needed to use the corresponding Johnson and Thuan-Gunn effective flux (e.g Fukugita et al. 1995). The accuracy of their photometry ranges from 0.1 mag to 0.5 mag from the brighter ($B \sim 20$ mag) to the fainter ($B \sim 26$ mag) objects. The spectroscopic data lacks the required quality needed to perform an accurate analysis of the age-metallicity indicators, like the equivalent widths of $H\beta$ and Mgb , but they provide high quality redshift determinations.

Ziegler et al. (2001) reported on multislit moderate-resolution spectroscopic observations of 48 color-selected early-type members of the cluster. They also present high-quality multiband photometry in 4 bands (U , B , V and I), derived from ground-based observations, and a morphological analysis of 19 of the 48 galaxies based on HST/WFPC2 observations (F702W-band, $\sim R$ -band). Finally, Smail et al. (2001) present a photometric study of the ages and metallicities of 81 early-type cluster candidates (33 with confirmed

redshifts), based on ground-based K -band and HST/WFPC multiband images, in the F450W, F606W and F814W-bands. In both cases, their photometric data were calibrated in the Vega-based system. Many other studies have targeted this cluster since its redshift confirmation by Kristian et al. (1978), and the early photometric studies by Butcher et al. (1983). However, in this paper we only use the photometric and spectroscopic data of the articles listed above.

Figure 2 shows a greyscale of the combined HST/ACS F850LP-band image, together with labels indicating the location of the galaxies studied by Le Borgne et al. (1992) (orange stars), Ziegler et al. (2001) (blue squares) and Smail et al. (2001) (red crosses). The location of the confirmed cluster members sampled by our IFS data are also indicated (green circles). As we will see below, most of them have not been previously targeted by any spectroscopic survey.

2.3 The depth of our IFS data

To obtain a rough estimate of the depth of our IFS data, we compared them with available deep optical images. Figure 3 shows a three-color image created by coadding the flux of the final datacube through three broad-bands corresponding approximately to B , R and I (left panel), together with a similar image created using the previously described HST/ACS dataset. It is interesting to note the similarities between the two images, despite the fact that our datacube has a final FWHM for point-like sources of $\sim 2.5''$, much larger than the one from the ACS. Based on the I -band magnitude of the faintest detected object, we roughly estimate the detection limit for our IFS data $I_{lim} \sim 22.4$ mag. However, we only get high enough quality spectra for the proposed study for objects brighter than $I < 21.5$ mag (signal-to-noise ratio $> 5\sigma$ per spectral pixel), as we will see below. This limit is far beyond previous spectroscopic studies on this cluster, around $I_{lim} \sim 18.7$ mag (Ziegler et al. 2001).

Table 2. Summary of the photometric analysis.

ID	RA	DEC	B_{475}	V_{555}	R_{625}	I_{775}	z_{850}
1	248.9537297	+66.2117906	18.09±0.02	17.29±0.02	16.52±0.01	15.85±0.01	15.44±0.01
247	248.9853560	+66.1981066	18.73±0.03	17.94±0.02	17.14±0.02	16.44±0.01	16.08±0.02
169	248.9870850	+66.1850276	18.86±0.03	18.09±0.03	17.34±0.02	16.70±0.02	16.19±0.02
512	248.9569254	+66.2059389	18.92±0.03	18.32±0.03	17.51±0.02	16.80±0.02	16.44±0.02
554	248.9546845	+66.2094133	19.53±0.04	18.87±0.04	18.26±0.03	17.56±0.03	17.00±0.03
172	249.0078962	+66.2089431	19.22±0.04	18.46±0.03	17.67±0.02	16.96±0.02	16.47±0.02
501	248.9646342	+66.2088796	19.40±0.04	18.67±0.04	17.93±0.03	17.12±0.02	16.61±0.03
561	248.9762849	+66.2328158	19.33±0.04	18.62±0.04	17.92±0.02	17.17±0.02	16.65±0.03
189	248.9961745	+66.2011969	19.57±0.05	18.75±0.04	17.93±0.02	17.27±0.02	16.78±0.03
103	249.0154109	+66.1939177	19.50±0.05	18.72±0.04	17.91±0.02	17.25±0.02	16.68±0.03
132	249.0082842	+66.1973755	19.57±0.05	18.76±0.04	17.95±0.03	17.27±0.02	16.73±0.03
555	248.9468602	+66.2111799	19.92±0.05	19.19±0.05	18.44±0.03	17.69±0.03	17.14±0.03
201	249.0162635	+66.2230941	19.61±0.05	18.83±0.04	18.09±0.03	17.39±0.02	16.89±0.03
2	248.9453711	+66.2204800	19.89±0.06	19.10±0.05	18.35±0.03	17.65±0.03	17.12±0.03
256	248.9833226	+66.1968621	19.89±0.05	19.20±0.05	18.46±0.03	17.80±0.03	17.20±0.04
509	248.9602122	+66.2050146	20.20±0.06	19.44±0.05	18.43±0.03	17.73±0.03	17.26±0.04
349	248.9959951	+66.2142513	20.00±0.06	19.23±0.05	18.54±0.03	17.77±0.03	17.27±0.04
126	249.0253609	+66.2126854	19.90±0.06	19.12±0.05	18.41±0.03	17.73±0.03	17.26±0.04
570	248.9630196	+66.2194216	20.11±0.06	19.35±0.05	18.62±0.04	17.93±0.03	17.41±0.04
523	248.9871643	+66.2387374	---	---	---	---	17.39±0.04
604	248.9528976	+66.2162360	19.41±0.04	18.95±0.04	18.35±0.03	17.94±0.03	17.49±0.04
599	248.9437771	+66.2056763	20.23±0.07	19.40±0.05	18.65±0.04	18.00±0.03	17.46±0.04
658	248.9415886	+66.2137478	20.29±0.07	19.53±0.06	18.80±0.04	18.11±0.04	17.59±0.04
337	248.9878980	+66.2037120	20.53±0.08	19.76±0.06	18.97±0.04	18.35±0.04	17.64±0.05
596	248.9468067	+66.2083220	20.68±0.08	19.83±0.07	19.07±0.05	18.37±0.04	17.77±0.05
462	248.9709853	+66.2100529	20.30±0.07	19.49±0.06	18.85±0.04	18.21±0.04	17.86±0.05
471	248.9564109	+66.1951060	20.64±0.08	19.83±0.07	19.03±0.04	18.46±0.04	17.86±0.05
302	248.9999910	+66.2116528	20.68±0.08	19.91±0.07	19.18±0.05	18.53±0.04	17.79±0.05
388	248.9849322	+66.2108143	20.41±0.07	19.74±0.06	19.08±0.05	18.48±0.04	17.97±0.05
449	248.9708088	+66.2082924	20.62±0.56	19.85±0.10	19.05±0.04	18.39±0.04	18.01±0.05
72	249.0309189	+66.1939739	---	---	---	---	17.89±0.05
408	248.9916711	+66.2220150	20.62±0.08	19.91±0.07	19.19±0.05	---	17.95±0.05
95	249.0389514	+66.2155899	20.96±0.09	20.24±0.08	19.53±0.06	18.87±0.05	18.33±0.06
798	249.0240772	+66.1820752	---	---	---	---	18.41±0.07
511	248.9579508	+66.2047618	20.35±0.11	19.72±0.10	19.25±0.06	18.68±0.06	18.51±0.07
493	248.9754372	+66.2174786	21.44±0.12	20.74±0.10	19.99±0.07	19.33±0.07	18.64±0.07
643	248.9401830	+66.2084529	21.45±0.12	20.67±0.10	19.97±0.07	19.29±0.06	18.59±0.07
329	249.0093949	+66.2250084	21.19±0.11	20.49±0.09	19.69±0.06	19.00±0.06	18.52±0.07
549	248.9519752	+66.2020070	21.33±0.11	20.65±0.10	19.94±0.07	19.23±0.06	18.76±0.08
632	248.9484012	+66.2157872	21.47±0.14	20.50±0.10	19.84±0.06	19.21±0.06	18.89±0.07
357	248.9817003	+66.2002660	21.85±0.14	20.54±0.09	19.73±0.06	19.05±0.06	18.53±0.07
560	248.9510744	+66.2127998	22.45±0.19	21.81±0.17	21.06±0.12	20.49±0.12	20.00±0.10
196	249.0143811	+66.2200223	21.71±0.13	20.99±0.12	20.26±0.08	19.57±0.07	19.01±0.09
384	248.9824979	+66.2061905	21.46±0.12	20.83±0.11	20.17±0.08	19.57±0.07	19.09±0.09
411	248.9954237	+66.2254124	21.75±0.14	20.99±0.12	20.27±0.08	19.56±0.07	18.91±0.08
603	248.9619939	+66.2146043	21.83±0.14	21.10±0.12	20.37±0.09	19.73±0.08	19.13±0.09
533	248.9615077	+66.2088133	22.07±0.15	21.39±0.14	20.60±0.10	19.78±0.08	19.30±0.09
619	248.9427500	+66.2068096	21.94±0.15	21.21±0.13	20.58±0.09	19.93±0.09	19.30±0.10
484	248.9624573	+66.2014471	21.84±0.14	21.24±0.13	20.52±0.09	19.97±0.09	19.50±0.10
153	249.0133589	+66.2067467	21.83±0.14	21.16±0.13	20.41±0.09	19.79±0.08	19.24±0.10
513	248.9540625	+66.2052672	22.31±0.23	21.58±0.15	20.64±0.18	19.64±0.18	19.04±0.09
507	248.9578870	+66.2008693	22.40±0.20	21.68±0.18	21.03±0.12	20.39±0.11	19.84±0.13
431	248.9752130	+66.2068778	20.89±0.09	20.60±0.10	20.27±0.08	19.97±0.09	19.78±0.13
659	248.9460977	+66.2174923	23.69±0.34	22.91±0.29	22.14±0.20	21.46±0.18	20.81±0.17
575	248.9613337	+66.2169292	22.94±0.24	22.05±0.20	21.43±0.15	20.79±0.13	20.36±0.17
574	248.9534579	+66.2081824	23.14±0.32	22.48±0.28	21.74±0.16	21.02±0.14	20.47±0.16

3 ANALYSIS AND RESULTS

3.1 Photometric analysis

We used the previously described HST/ACS images to obtain homogeneous multiband photometry for all the detected

object in field of Abell 2218. This homogeneous photometric dataset is fundamental to estimate the accuracy of the the spectrophotometric calibration of our IFS data and to study the stellar populations of the galaxies in the cluster. We use **SExtractor** (Bertin et al. 1996) to detect objects

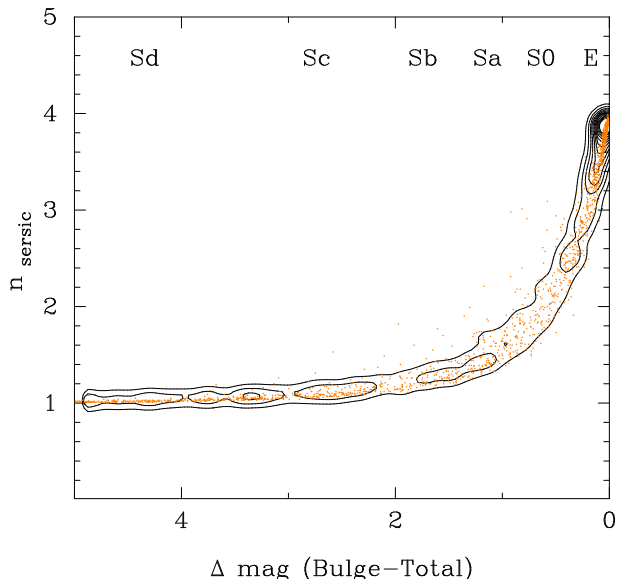


Figure 4. Results from the simulations. Solid-dots show the recovered Sérsic indices of the simulated galaxies as a function of the magnitude difference between the bulge and total components (Δmag). Overplotted contours show the density distribution of the plotted points.

in the images up to 15σ over the sky (20 connected pixels with a signal-to-noise of at least 2σ each one). This limit is very relaxed, and most probably we are losing many real faint objects by using it. However, we are not interested in the faintest targets, most probably high- z objects or arc-lenses (see Fig 1), but only in the cluster members. For each detected target we obtained aperture photometry in each band, using the `MAG_BEST` parameter derived by `SExtractor`. The little variations of the HST/ACS PSF compared to the size of our targets of interest guarantees homogeneous photometric dataset. Table 2 lists the results from this analysis for the 59 galaxies confirmed to be cluster members, using the published data listed above or the results from our spectroscopic survey (see below). For each target it includes the `SExtractor` ID, the coordinates (RA and DEC), and the photometry in each band plus errors. Due to the change of orientation and slightly different pointing of the individual HST/ACS frames, the F850LP-band covers a slightly larger area than the images in the other bands, and some of the objects were only detected in this band.

3.2 Morphological analysis

One of the goals of the present study is to determine the stellar populations of galaxies in the cluster as a function of their morphologies, in order to understand their origin and evolution. To achieve this goal we performed a morphological analysis of the HST/ACS F850LP images, the deepest of our dataset, following the prescriptions presented in Coe et al. (2006), where similar images were analyzed. This analysis recovers, for each galaxy, the Sérsic index, the integrated magnitude, the effective radius, the ellipticity, the position angle, and the asymmetry index.

For undisturbed galaxies the Sérsic index n correlates fairly well with morphological type (e.g. Andreidakis et al.

1995; Bell et al. 2004), in the sense that galaxies with high n have higher central concentrations (i.e., bulge dominated galaxies) than galaxies with low n (i.e., disk dominated galaxies). Less well behaved galaxies, including mergers and irregulars, generally do not have well defined Sérsic indices. Fortunately these galaxies can generally be weeded out (or selected for) by measuring their large asymmetries (e.g. Conselice et al. 2003).

In summary the morphological analysis consists of the following steps: First we use `SExtractor` (Bertin et al. 1996) to detect galaxies in the combined F850LP-band image. For each detected galaxy we recover the physical and image coordinates (RA,DEC, X and Y), the integrated magnitude (`mag_best`), the scale-length (r_{50}), the position angle and the ellipticity. Then, we create a postage stamp $5 \times r_{50}$ on a side, for the brightest galaxy. Within that postage stamp, neighbouring galaxies are masked out using ellipses, each ellipse given a minor axis length $b = 2 \times r_{50}$ for that galaxy. Using `galfit` (Peng et al. 2002), the brightest galaxy is fitted to a single component Sérsic model $\Sigma(R) = \Sigma_e \times \exp(-\kappa_n[(R/R_e)^{1/n} - 1])$, where R_e is the effective or half-light radius, Σ_e is the effective surface density, $\Sigma(R)$ is the surface density as a function of radius and $\kappa = \kappa(n)$ is a normalization constant. The fit is constrained to $0.2 < n < 8$ and $0.3 < R_e < 500$ pixels, and the centroid is confined to within 2 pixels of the position derived by `SExtractor`. As initial guesses for the `galfit` parameters, we use the `SExtractor` output parameters. Lacking estimates for the Sérsic index from `SExtractor`, we start all fits with $n = 1.5$. `galfit` convolves the model with the required PSF. Prior to the fit, we created a PSF image by combining postage stamps of unsaturated point-like objects extracted from the combined F850LP-band image.

Having been calculated for the brightest galaxy, the Sérsic model is subtracted from the F850LP-band image. This subtraction benefits the subsequent modelling of fainter nearby galaxies. We then proceed to model the second brightest galaxy, and continue in order of decreasing brightness, modelling and subtracting every galaxy in the `SExtractor` catalogue. `galfit` is able of simultaneous fit several targets, producing reasonable results, in most of the cases. However, in this case the fitting process is dominated by the brighter targets, and flux of the fainter ones is more poorly recovered. We performed extensive tests before adopting the described procedure. In addition, we determine the asymmetry index (A), following the prescriptions in Coe et al. (2006). Of the 802 objects detected by `SExtractor` in the F850LP-band image brighter than $z < 26.5$ mag, we applied `galfit` to the 241 galaxies brighter than $z < 22.5$ mags. The error in the derived Sérsic index is restricted to a range of ± 0.25 , based on the simulations presented in Coe et al. (2006), and therefore a morphological segregation based on that parameter is reliable. The remaining galaxies are far beyond the depth of our spectroscopic data, and therefore excluded. Table 3 lists the resulting fitted parameters and their uncertainties for the 59 galaxies confirmed to be cluster members, using the published data listed above or the results from our spectroscopic survey (see below). It includes, for each galaxy, the `SExtractor` identification, the χ^2/ν of the fitting procedure, the z -band magnitude, the effective radius (R_e), the axis ratio (a/b), the position angle (θ), the Sérsic index (n_s) and the Asymmetry

index (A). The listed errors were estimated based on the results of the simulations presented in Coe et al. (2006). The error in the Asymmetry index is difficult to quantify for individual objects, however, based on the quoted simulations, we estimate it to be lower than ~ 0.1 for the galaxies of our sample. Of all these galaxies, only one has a strong Asymmetry index (~ 0.8). This galaxy is covered by the field-of-view of our IFS data, and it will be discussed later in detail.

3.3 The Sérsic indices and the Hubble sequence

Our morphological classification scheme is based on the Sérsic index of the galaxy profile. We consider this automatic classification scheme more straight forward, easy to reproduce, and less subjective than the classical *by-eye* classification (read Wolf et al. 2005, for an illustration of the problem). However, most of the previous studies on the morphologies of galaxies in clusters are based on *by-eye* classifications following the Hubble scheme (Hubble 1926), revised by de Vaucouleurs et al. (1976). Normally, they subdivide the galaxies in their different Hubble types, or at least in three groups: pure spheroidals (E-type), lenticulars (S0), and spirals (L-type) (e.g. Fasano et al. 2000; Poggianti et al. 2001; Ziegler et al. 2001; Smail et al. 2001). In order to compare with previous results it is necessary to determine to which type our galaxies, based on their Sérsic indices, correspond.

As we indicated above, Andredakis et al. (1995) show that there is a correlation between the Sérsic index and morphological type. However, here we need to determine how these parameters correlate for our dataset. For doing so, we follow Fasano et al. (2000) and create a set of simulated galaxies. Their magnitudes, scale-lengths, position angles and ellipticities are extracted from the previously described morphological catalogue of 241 galaxies. For each entry in the morphological catalogue 20 galaxies were simulated, each one with a different bulge-to-disk ratio, ranging randomly from 0.01 (almost a pure disk) to 1000 (almost a pure spheroidal). Each galaxy image was created using `galfit`, with a two components Sérsic model, one with $n_s=4$ for the bulge and another with $n_s=1$ for the disk, convolving them with the same PSF used in the morphological analysis. Finally, `noise` was added following the prescription presented in Coe et al. (2006) and Sánchez et al. (2004c) for simulating ACS images, to resemble as much as possible the original F850LP-band image.

The same morphological analysis described in the previous section was performed for each of the simulated galaxy images, fitting them to a single component Sérsic model. Finally we end up with ~ 5000 simulations comprising the recovered Sérsic index for a certain bulge-to-disk ratio. Simien & de Vaucouleurs (1986) show the typical bulge-to-disk ratios for the different families of galaxies in the revised Hubble sequence. In particular, they present the mean fractional luminosity of the spheroidal component of the galaxies and its corresponding magnitude difference for each galaxy type. Figure 4 shows the Sérsic indices of the simulated galaxies as a function of these magnitude differences (Δmag). The differences for various families of galaxies along the Hubble sequence are indicated (extracted from Simien & de Vaucouleurs 1986). Based on this figure we adopted the following scheme to morpholog-

ically classify galaxies based on the Sérsic indices: galaxies with $n_s > 2.5$ are considered spheroidals (E-type), galaxies with $1.75 < n_s < 2.5$ are considered intermediate type (mostly S0's, but strongly contaminated by other families of bulge-dominated spirals, like Sa and Sb), and galaxies with $n_s < 1.75$ are considered spirals (L-type).

This classification scheme is based on the fair correlation between the bulge-to-total luminosity ratio and the hubble type of a galaxy Simien & de Vaucouleurs (1986). However we may admit that some degree of contamination is expected among the different morphological subgroups due to the dispersion in this correlation. Although we can clearly distinguish between pure spheroidals (E-type) and spirals (L-type), the subgroup of intermediate type is most probably less accurately defined, with considerable contaminations from both extreme subgroups. Another source of criticism about the adopted scheme is the fact that some dwarf elliptical galaxies shown low Sérsic indices (e.g., Barazza et al. 2003). Although in galaxy surveys without morphological pre-selections most of the galaxies with low Sérsic indices are spiral galaxies Andredakis et al. (1995), the contamination from dwarf ellipticals could be a potential problem in the study of galaxy clusters. To address this problem we perform a visual inspection of the 29 galaxies with $n_s < 1.75$ listed in Table 2 and 3 (ie., the ones classified as spirals) using the previous described HST/ACS images. Only 2 of these 29 galaxies ($\sim 7\%$) could be classified as dwarf spheroidals based on this visual inspection. However both of them are nearby brighter galaxies, and their low surface brightness areas (like disk structures) are not clearly distinguished. In any case, the possible contamination by dwarf spheroidal galaxies is expected to be marginal. The remaining galaxies show clear evidence of disk structures. Taking into account these caveats we consider that the adopted classification scheme is valid within the context of this study.

3.4 Spectra extraction

To deblend and extract the integrated spectra of each individual galaxy in the field we used a technique for 3D crowded field spectroscopy developed by ourselves (Sánchez et al. 2004b; García-Lorenzo et al. 2005; Sánchez et al. 2006). The technique is an extension to IFS of `galfit` (Peng et al. 2002), that we named `galfit3d`. It consists of a deblending of the spectrum of each object in the datacube by fitting of analytical models. IFS data may be understood as a set of adjacent narrow-band images, with the width of the spectral pixel. For each narrow-band image it is possible to apply modelling techniques developed for 2D imaging, like `galfit`, and extract the morphological and flux information for each object in the field at each wavelength. The spectra of all the objects is extracted after repeating the technique through the datacube. We have already shown that the use of additional information to constrain the morphological parameters increases the quality of the recovered spectra (Sánchez et al. 2006). With that purpose we used the morphological parameters previously derived from the HST/ACS F850LP-band image.

We create a 2D image by coadding the flux through the usefull wavelength range (4650–8000 Å) covered by our datacube. After this, we cross-checked by eye this image, looking for those galaxies detected in the F850LP-band for

Table 3. Summary of the morphological analysis.

ID	χ^2/ν	z_{850}	R_e (")	a/b	θ	n_s	A
1	0.017	16.10±0.02	12.06±0.05	0.49±0.01	37± 4	1.63±0.06	0.093
247	0.023	16.21±0.02	5.18±0.05	0.85±0.01	51± 4	1.88±0.06	0.175
169	0.024	17.07±0.02	1.66±0.06	0.49±0.02	89± 4	1.48±0.07	0.043
512	0.033	17.20±0.02	1.51±0.06	0.77±0.02	-37± 8	2.03±0.07	0.156
554	0.034	17.37±0.02	0.63±0.06	0.80±0.02	-10± 5	1.80±0.07	0.321
172	0.016	16.84±0.02	1.64±0.06	0.82±0.01	-46± 9	2.95±0.06	0.056
501	0.026	15.92±0.02	0.81±0.05	0.84±0.01	50± 5	2.86±0.05	0.045
561	0.020	17.25±0.02	1.52±0.06	0.69±0.02	-81±12	1.47±0.07	0.081
189	0.019	17.14±0.02	2.69±0.06	0.90±0.02	-59±10	3.93±0.07	0.088
103	0.011	16.93±0.02	1.17±0.05	0.94±0.01	-26± 5	2.69±0.06	0.042
132	0.018	17.28±0.02	1.20±0.06	0.46±0.02	-6± 5	2.78±0.07	0.058
201	0.027	17.49±0.02	0.89±0.06	0.50±0.02	-61±10	1.91±0.07	0.132
2	0.013	17.43±0.02	0.96±0.06	0.80±0.02	-16± 5	2.63±0.07	0.050
256	0.022	17.64±0.02	0.51±0.06	0.85±0.02	75± 5	1.74±0.07	0.078
509	0.028	17.46±0.02	1.09±0.06	0.66±0.02	-33± 7	3.19±0.07	0.129
349	0.016	17.98±0.02	0.86±0.07	0.70±0.02	71± 4	2.23±0.07	0.077
126	0.033	17.44±0.02	0.68±0.06	0.95±0.02	-83±12	2.00±0.07	0.159
570	0.020	18.32±0.03	1.15±0.08	0.37±0.03	-63±10	1.81±0.08	0.054
523	0.018	17.78±0.02	0.70±0.07	0.57±0.02	-88±13	1.74±0.07	0.047
73	0.018	17.90±0.02	0.83±0.07	0.81±0.02	38± 5	2.02±0.07	0.077
604	0.021	18.09±0.03	1.13±0.08	0.44±0.03	84± 4	0.72±0.08	0.129
599	0.019	17.76±0.02	1.04±0.07	0.91±0.02	20± 5	3.94±0.07	0.051
658	0.016	17.87±0.02	1.01±0.07	0.88±0.02	51± 6	2.69±0.07	0.081
337	0.015	17.96±0.02	0.59±0.08	0.78±0.02	5± 4	2.49±0.07	0.050
596	0.015	18.96±0.03	0.65±0.09	0.64±0.05	58± 6	2.13±0.08	0.067
210	0.041	18.19±0.03	0.47±0.08	0.59±0.03	-21± 6	2.03±0.08	0.823
462	0.021	18.21±0.03	1.35±0.08	0.84±0.03	-21± 7	2.35±0.08	0.102
471	0.015	18.12±0.03	0.97±0.08	0.89±0.03	3± 5	2.11±0.08	0.118
302	0.014	18.14±0.03	0.48±0.08	0.93±0.03	5± 6	2.01±0.08	0.048
388	0.015	18.25±0.03	0.71±0.08	0.76±0.03	45± 5	1.68±0.08	0.065
449	0.021	18.57±0.03	1.60±0.08	0.87±0.04	89± 6	1.03±0.08	0.316
72	0.019	18.64±0.03	0.73±0.09	0.44±0.04	72± 5	2.13±0.08	0.057
408	0.017	18.59±0.03	0.72±0.08	0.74±0.04	-12± 6	1.46±0.08	0.152
95	0.015	18.41±0.03	0.63±0.08	0.85±0.03	80± 6	1.45±0.08	0.062
798	0.020	19.02±0.04	0.88±0.10	0.45±0.06	9± 5	0.81±0.09	0.068
511	0.029	18.74±0.03	0.57±0.09	0.53±0.04	-67±12	2.35±0.08	0.169
493	0.018	18.99±0.03	0.45±0.09	0.72±0.06	-42± 9	1.56±0.08	0.058
643	0.014	19.09±0.04	0.45±0.10	0.99±0.06	84±13	1.74±0.09	0.094
329	0.015	18.71±0.03	0.76±0.09	0.77±0.04	41± 6	1.46±0.08	0.071
549	0.012	19.04±0.04	0.63±0.10	0.95±0.06	-35± 9	1.77±0.09	0.067
632	0.017	19.03±0.04	0.37±0.10	0.73±0.06	-82±13	1.49±0.09	0.102
357	0.018	18.70±0.03	0.60±0.09	0.67±0.04	-9± 6	1.07±0.08	0.184
560	0.049	18.39±0.03	0.17±0.08	0.87±0.03	-74±12	0.53±0.08	0.469
503	0.013	19.33±0.04	0.83±0.10	0.80±0.07	13± 6	0.97±0.09	0.133
196	0.016	19.14±0.04	0.51±0.10	0.67±0.06	-8± 6	1.38±0.09	0.079
384	0.017	19.53±0.06	0.77±0.12	0.43±0.08	-45±10	1.29±0.09	0.067
411	0.010	18.86±0.03	0.39±0.09	0.96±0.04	-81±13	1.88±0.08	0.080
603	0.012	19.59±0.06	0.49±0.12	0.96±0.08	43± 9	1.19±0.09	0.059
533	0.015	18.87±0.03	0.27±0.09	0.94±0.04	65± 9	1.44±0.08	0.045
619	0.015	19.55±0.06	0.41±0.12	0.74±0.08	5± 6	1.29±0.09	0.069
484	0.017	19.71±0.06	0.75±0.13	0.51±0.08	36± 5	1.18±0.09	0.078
153	0.013	19.69±0.06	0.69±0.13	0.72±0.08	-76±13	1.34±0.09	0.062
513	0.024	20.04±0.08	1.15±0.17	0.50±0.10	39±10	2.31±0.10	0.194
507	0.013	20.27±0.09	0.38±0.18	0.85±0.11	74±10	1.31±0.10	0.061
431	0.014	20.20±0.09	1.10±0.18	0.85±0.11	32±11	0.89±0.10	0.218
803	0.017	21.21±0.16	0.67±0.26	0.86±0.15	64±17	0.40±0.15	0.240
659	0.019	20.66±0.11	0.25±0.22	0.81±0.12	-83±17	1.68±0.12	0.085
575	0.010	20.86±0.09	0.75±0.24	0.85±0.12	-40±13	1.39±0.13	0.119
574	0.011	20.49±0.06	0.27±0.22	0.84±0.11	-89±18	1.15±0.12	0.073

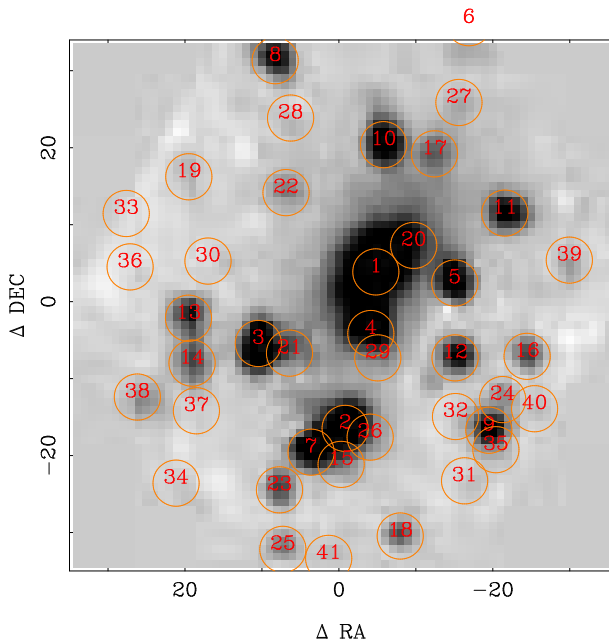


Figure 5. Grayscale representation of the 2D image obtained by coadding the flux from the datacube through all the covered wavelength range (4650-8000 Å). The circles indicate the location of the detected galaxies in the datacube, together with a number indicating the label code used to identify them.

which we had performed a morphological analysis. We detect 41 objects (40 galaxies and 1 star) in the collapsed 2D image, out to $z < 23$ mag. The gravitational arc-lenses were excluded since their study is out the scope of the current work. Figure 5 shows a greyscale of the coadded 2D image derived from the datacube, together with an identification label at the location of each of the detected objects.

As we mentioned before, we use the previously derived morphological parameters for each galaxy to extract its integrated spectrum by modelling each galaxy in the datacube with `galfit3d`. We use the same model that was used to fit the F850LP-band image, with all the morphological parameters fixed, and fitting only the flux at each wavelength. For each wavelength, we created a PSF using postage stamp images of the only field-star in the field-of-view of our IFS data. As in the previous morphological analysis, the 3D fit was performed in a sequential way. We first extracted the spectrum of the brightest galaxy, the central cD, masking the neighbouring galaxies. Once extracted, its 3D model was subtracted to the original datacube, and the spectrum of the second brightest galaxy was extracted. The process continued iteratively until the faintest galaxy spectrum was extracted. The individual spectra are shown in Appendix A. All of them are background limited. Thus, the signal-to-noise ratio can be estimated from the background-noise level. We used the variations in the sky spectrum in each sky-fiber to determine the level of background noise. In this way, we estimated that the signal-to-noise of the extracted spectra range between ~ 1000 and ~ 5 per spectral pixel for the brightest and faintest targets. The signal-to-noise ratio is affected strongly by the sky-emission lines (see Fig. 1), where it drops to less than $\sim 3\sigma$ even for the brightest targets, respectively. The effect is more severe in the wavelength

range $\lambda > 7200\text{Å}$ where many sky-emission lines happen to be blended.

The procedure relies on the assumption that the morphological parameters do not change substantially as a function of the wavelength, something which it is not completely true, since color gradients are expected in all the galaxies. But, if they change, we expect this effect to have a minim impact in the photometry derived with `galfit`. Thus, if we use the morphological parameters derived by applying `galfit` to the F850LP-band and we force the fitting procedure to use them for deriving the photometry at any other band, the recovered flux should be basically the same as when we let `galfit` fit these parameters freely. Although our previous experiments shown that this is the case (e.g. García-Lorenzo et al. 2005), we have also tested this hypothesis here, as described in Appendix B. In any case, the method is not strongly sensitive to this assumption, as described in Sánchez et al. (2006). In principle, it is possible to perform the extraction procedure using the parameters derived from the morphological analysis as an initial guess, and letting `galfit` to derive the correct ones for each wavelength. In this case, the recovered spectra are noisier and in the residual datacube there is clear evidence of not correctly extracted structure.

3.5 Redshift determination

We determined the redshift of each detected galaxy in the field-of-view of our IFS data by comparing its spectrum with synthetic models for single stellar populations obtained from Bruzual & Charlot (2003). We will describe later in detail which models were used. We manually tuned the redshift of the model matching the different absorption features, including the Balmer lines ($H\beta$, $H\gamma$, $H\delta$), the different Fe and Mg lines covered by our spectral range, as well as spectral features, like the 4000Å break. Due to the spectral resolution of our IFS data, and the signal-to-noise of our targets, we do not expect to have an accuracy better than 0.001 in the redshift determination. We derived reliable redshifts for 31 galaxies, 28 of them at the redshift of the cluster ($z = 0.17 \pm 0.2$), one is a foreground galaxy ($z = 0.104$), and other two are background galaxies (both at $z \sim 0.426$). Table 4 lists the derived redshifts together with the identifications shown in Fig. 5 (that we will use throughout this paper) and the `SExtractor` identification listed in Table 3 to allow for direct comparison.

Eleven of the 28 galaxies were studied before by Le Borgne et al. (1992). The redshifts derived from our data are coincident with the reported in this article within the expected errors ($\sigma_z \sim 0.001$). We derive new redshifts for 17 galaxies, all of them compatible with the redshift of the cluster. These new galaxies have been included in the Table 3. In total, the final sample of cluster members (28) is comparable with that one of previous similar studies, but with the advantage that no sample has been selected: our sample is complete within the field-of-view of our IFS data down to our detection limit. Of these galaxies, only 6 have been previous studied with enough quality spectroscopy to derive the properties of their stellar populations (Ziegler et al. 2001). Therefore, our sample will increase significantly our knowledge of the core of the cluster.

Table 4. Summary of the parameters derived from the spectra

IFU ID	SEx. ID	z	H β	Mgb	Age Gyr	Met Z	Mass $10^{10}M_{\odot}$
1	1	0.174	<i>1.6±0.1</i>	<i>3.0±0.1</i>	9.8±2.8	0.019±0.011	102.1±2.6
2	512	0.179	2.1±0.1	3.4±0.1	12.0±3.4	0.025±0.014	74.6±2.8
3	501	0.163	1.1±0.1	4.2±0.2	12.9±3.6	0.046±0.026	39.5±2.0
4	554	0.175	2.8±0.1	3.6±0.1	12.1±3.4	0.025±0.014	67.9±3.3
5	555	0.181	1.4±0.1	4.1±0.2	11.6±3.2	0.032±0.018	36.2±2.2
6	2	0.181	1.5±0.6	6.1±0.9	12.7±3.6	0.045±0.025	75.7±4.6
7	509	0.184	<i>1.0±0.1</i>	<i>3.0±0.1</i>	9.9±2.8	0.019±0.011	17.2±1.2
8	570	0.184	<i>1.5±0.2</i>	<i>2.3±0.7</i>	12.7±3.6	0.045±0.025	39.9±2.7
9	599	0.163	1.5±0.1	4.4±0.2	9.6±2.7	0.019±0.011	10.5±0.8
11	658	0.172	2.2±0.1	3.9±0.1	9.5±2.7	0.018±0.010	11.5±0.8
12	596	0.174	1.4±0.1	4.9±0.1	12.4±3.5	0.024±0.013	13.6±1.2
13	462	0.179	3.2±0.1	2.7±0.2	4.5±1.3	0.018±0.010	7.8±0.6
14	449	0.178	2.7±0.1	2.8±0.2	5.2±1.4	0.009±0.005	4.5±2.3
15	511	0.162?	<i>1.0±0.2</i>	<i>2.5±0.2</i>	9.5±2.7	0.001±0.001	2.2±0.3
16	643	0.167	<i>1.2±0.1</i>	<i>0.7±0.3</i>	9.7±2.7	0.019±0.011	4.1±0.5
17	632	0.179	2.8±0.3	3.0±0.2	3.5±1.0	0.009±0.005	2.1±0.3
18	549	0.172	—	<i>3.5±0.3</i>	5.2±1.4	0.009±0.005	2.8±0.4
20	560	0.180	<i>2.2±0.2</i>	<i>0.7±0.4</i>	9.7±2.7	0.019±0.011	1.8±0.3
21	533	0.171	<i>1.2±0.3</i>	<i>1.8±0.3</i>	11.5±3.2	0.031±0.018	4.5±0.7
22	603	0.171	—	<i>2.7±0.3</i>	5.8±1.6	0.003±0.002	1.0±0.2
24	619	0.159	3.1±0.2	2.8±0.5	11.4±3.2	0.006±0.003	1.5±0.2
25	484	0.174	<i>1.2±0.5</i>	<i>0.9±0.3</i>	4.2±1.7	0.007±0.004	1.0±0.2
26	513	0.180	3.8±0.4	—	7.1±2.0	0.019±0.011	2.1±0.5
27	659	0.168	—	—	12.8±3.6	0.045±0.025	1.8±0.6
28	575	0.168	—	—	12.7±3.6	0.044±0.025	3.6±0.9
29	574	0.168	2.3±0.7	—	9.7±2.7	0.008±0.004	0.6±0.2
38	431	0.170	—	<i>1.2±0.4</i>	0.3±0.1	0.007±0.004	0.1±0.1
41	507	0.168	—	—	5.8±1.6	0.007±0.004	0.6±0.1

Uncertain values are written in italic.

3.6 The color-magnitude diagram

Figure 6 shows the rest-frame $B-V$ vs. M_V color-magnitude diagram for those cluster members listed in Table 2, derived from the HST/ACS based photometric data described above. The absolute magnitudes were corrected for cosmological effects and we applied a k -correction based on the same SSP synthetic model. For each synthetic SSP model (described below) we derived the expected $B-V$ colors at the average redshift of the cluster and in the rest-frame, deriving at the same time the V -band k -correction. An average relation between the observed and rest-frame colors and the k -correction was derived, and applied to the data shown in Fig. 6. Red solid circles indicate galaxies with Sérsic index $n > 2.5$ (E-type), while green stars indicate those with $n < 1.75$ (L-type). Orange solid squares indicate galaxies with Sérsic indices in between those values, corresponding to intermediate galaxies. The cD galaxy is indicated with an orange open cross, being the brightest object in the field. We prefer to label it with a different symbol since it is well known that cD galaxies do not follow a Sérsic profile of any index, showing a flatter and more extended light profile in the outer regions (e.g. Oemler 1976). Open circles indicate the galaxies within the field-of-view of our IFS, with redshifts listed in Table 4. The big open square indicates the only galaxy with a high Asymmetry index.

3.6.1 Morphological segregation

To our knowledge this is the first time that a morphologically segregated color-magnitude diagram is shown for confirmed cluster members. In previous works (e.g. Smail et al. 2001) only cluster galaxy candidates have been shown. The morphologies, based on the Sérsic indices listed in Table 3, break down as: 11 E-type, 19 intermediate and 29 L-type. If we consider as E-type galaxies to be all the objects with $n > 1.75$, they represent only a $\sim 50\%$ of the total. For the complete subsample of galaxies covered within the IFU field-of-view, the morphologies breaks down as: 7 E-type, 8 intermediate and 13 L-type. Contrary to previous results (e.g. Ziegler et al. 2001; Smail et al. 2001) this indicates that the cluster population is not dominated by early-type galaxies, and there is an almost parity between early- and late-type galaxies.

Our approach to derive the morphologies is substantially different to in previous attempts, based on visual classifications. There is a considerable debate over the reliability of visual classifications of early-type galaxies (e.g. Dressler et al. 1997; Andreon 1998; Fabricant et al. 2000), and the ability to compare them with classifications based on profile analysis, like concentration and/or Sérsic indices. However, since there are no previous similar studies, we must compare with the existing ones. Ziegler et al. (2001) show visual morphological classifications of 19 of their 48 cluster members, based on WFPC/HST imaging. Their classification was performed by W. Couch, who classified them as 8 E,

1 E/S0, 5 S0, 3 SB/0, 1 Sa and 1 Sab. Taking together all the E-type galaxies (E, E/S0 and S0), they account for a $\sim 73\%$ of the total sample. Smail et al. (2001) presented morphological classification for 81 cluster candidates (33 with confirmed redshifts), based on the same analysis as Ziegler et al. (2001). Their morphologies break down as: 31 E, 3 E/S0, 28 S0, 5 Sa and 14 late-type spirals. Taking together all the E-type galaxies, they account for a $\sim 76\%$ of the total sample. Even taking into account the different methods used to derive the morphologies, and the difficulties to compare them, it is clear that both Ziegler et al. (2001) and Smail et al. (2001) found fewer L-type galaxies than what we are finding.

Ziegler et al. (2001) selected galaxies using the previously existing redshift catalogue from Le Borgne et al. (1992) and defining a region in the $UBVI$ colour space which was occupied by cluster members. Finally, only galaxies brighter than $I < 18.8$ mag were targeted by their spectroscopic survey. Although it was claimed that this selection places negligible restrictions on the stellar populations of the selected galaxies, and was made with the aim of rejecting the majority of background galaxies, it may have had an effect on the morphological segregation. The brightness cut in the I -band implies that all the observed galaxies are brighter than $M_V < \sim -19.5$ mag, assuming an average $V - I$ color of ~ 1.5 mag (Fukugita et al. 1995). If we apply such a cut in our sample (see Fig. 6), the morphologies break down as: 9 (7) E-type, 14 (5) S0's and 11 (2) L-type for the full (IFU) sample. This means a fraction of $\sim 68\%$ (86%) of E-type galaxies, in agreement with the results from Ziegler et al. (2001). Therefore, although visual classifications are not fully reproducible and may produce discrepancies in the morphological classification of individual objects, they agree with those ones based on Sérsic indices on a statistical base.

Smail et al. (2001) selected 81 cluster candidates based on a deep K_s -band survey ($K_s < 19$ mag), discarding those objects with clear stellar morphology, in too crowded areas and/or showing lensed morphologies. Assuming a $z - K_s$ color of ~ 3 mag for the reddest objects, based on their own results for $I - K_s$ and an average $z - I$ color of ~ 0.5 mag (Fukugita et al. 1995), they selected galaxies brighter than $z < \sim 22$ mag, a limiting magnitude similar to that of our IFU data. Therefore, a difference in the depth of both surveys is not the reason for the differences in the morphological segregation. We matched their cluster candidate sample with our full sample (listed in Table 3), finding 39 coincidences. For this subsample of confirmed cluster members the morphological segregation based on their analysis remains similar, with a $\sim 82\%$ of E-type galaxies. Therefore, possible contaminations from non cluster members are not the cause of the discrepancy. We examined the Sérsic indices of those 32 E-type galaxies. Of them, 10 have Sérsic indices lower than $n < 1.75$, being L-type galaxies following our scheme, and only 7 have $n > 2.5$. Thus, the discrepancy is most probably due to the different criteria adopted for classifying the objects, illustrating the risks of direct comparisons between both methods. Statistically speaking visual classification gives the same distribution of galaxy types as profile fitting: on average, their E-type galaxies have larger Sérsic indices ($n \sim 2.6$) than their L-type ones ($n \sim 1.7$). However, it is well known that one-to-one cross-checking both meth-

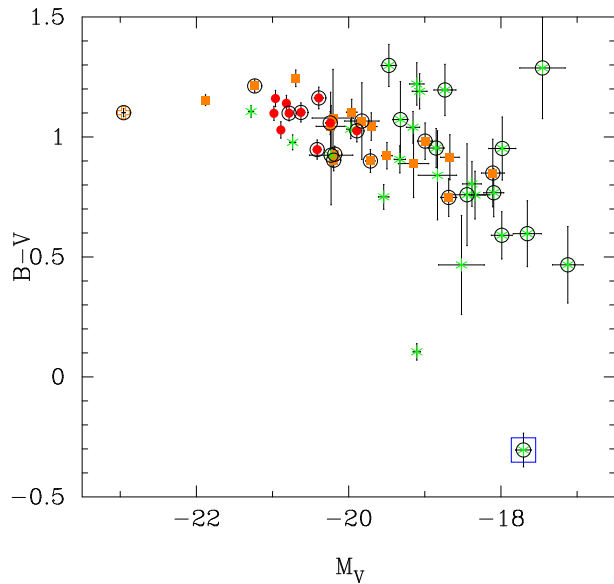


Figure 6. Rest-frame $B-V$ color distribution as a function of absolute magnitude M_V for those cluster members listed in Table 2. Red solid circles indicate galaxies with Sérsic index $n > 2.5$ (E-type), while green stars correspond to objects with $n < 1.75$ (L-type). Orange solid squares indicate lenticular galaxies, with Sérsic indices in between both values. The cD galaxy is indicated with an orange open cross, being the brightest object in the field. Open circles indicate the 28 galaxies within the field-of-view of our IFS. The big open square indicates the only galaxy with a high Asymmetry index.

ods give different results (e.g. Wolf et al. 2005), and profile analysis produces a more reliable and objective scheme for classifying objects.

3.6.2 Analysis of the CM diagram

The Color-Magnitude (CM) diagram contains extremely useful information to understand the nature of the cluster population. The $B - V$ color is related to both age (strongly) and metallicity (weakly) of the dominant stellar population of the galaxy. On the other hand, the V -band absolute magnitude can be related to the stellar mass. Figure 6 shows a bimodal distribution of early- and late-type galaxies in the CM diagram. E-type galaxies are (mostly) located in the brighter end of the distribution (no one is fainter than $M_V < \sim -20.5$ mag), covering a narrow range of colors ($1.9 < B - V < 2.2$). This is a well known feature of early type galaxies in clusters and it has been used for decades to select cluster candidates (e.g. Ziegler et al. 2001; Sánchez & González-Serrano 2002), and to trace the evolution of the older population of cluster galaxies (e.g. Aragon-Salamanca et al. 1993).

On the other hand, L-type galaxies are distributed across a wide range of magnitudes with the brightest almost as red as the early type galaxies, and the faintest bluer and covering a wider range of colors. For galaxies brighter than $M_V < -19.7$ mag there are no significant differences between the core members (galaxies in the IFU field-of-view), and the rest of the galaxies of the sample. For galaxies fainter than $M_V > -19.7$, it is found that the cluster core galaxies cover a wider range of colors, with more red galaxies. However, this difference may be due to a selection

effect of the galaxy samples obtained from the literature. As indicated in Section 4.3 two of the 29 galaxies classified as L-type could be spheroidals on the basis of a visual inspection of the HST/ACS images. Both of them have red colors, $B - V \sim 0.9$ mag. However they are not the redder L-type galaxies in their magnitude range. It is interesting to note here the location of the galaxy number 38 (IFU_{id}), the only one showing a high asymmetry, being the bluest galaxy of our sample. This galaxy, at the East in Fig. 2 and 3, is clearly identified as a merger in its latest stages, showing a clear tail to the South-West. Its spectrum, Fig. A1, shows strong H β , [OIII]4959,5007 and H α emission lines and weaker [NII]6548,6584, indicating a large amount of star formation. Its blue colors and spectrum also indicate the presence of an extremely young stellar population, far away from the global trend of the rest of the cluster members, as we will discuss below. Contrary to what is expected this galaxy is just at the nominal redshift of the cluster ($z = 0.17$, based on the emission lines), and considering its projected distance to the cluster center (assumed to be the cD), it is not likely to be a fly-by object. To our knowledge it has escaped the attention of previous studies, most probably because its morphology and color automatically exclude it as a cluster candidate. Our IFU data lack the required spatial and spectral resolution to perform a more detail study of its properties.

A brief comparison of the color-magnitude distribution of the different kind of galaxies in the cluster, segregated by their morphology, indicates that E-type galaxies are more massive and have older and more metal rich stellar populations. L-type galaxies cover a wider range of masses, ages and metallicities, with the more massive ones being similar to the E-type galaxies, and the less massive ones younger and metal poorer. This result indicates that a bulk star formation process at high redshift may not be the unique mechanism to explain the population of the galaxies in the cluster. We will investigate it further in the next sections.

3.7 Galaxies ages and metallicities

We obtained spectra of the individual galaxies in the cluster with the aim of comparing their global spectroscopic properties with their morphological ones in a relative way, ie., only within the cluster. It is well known that the spectral energy distribution (SED) of simple stellar populations (chemically homogeneous and coeval stellar systems) depends on a set of first principles (e.g., initial mass function, star formation rate, stellar isochrones, element abundance ratios), to make it possible to generate synthetic stellar populations from them. This technique, known as evolutionary synthesis modeling (e.g. Tinsley 1980), has been widely used to unveil the stellar population content of galaxies by reconciling the observed spectral energy distributions with those predicted by the theoretical framework. Unfortunately the variation of different physical quantities governing the evolution of stellar populations produce similar effects in the integrated light of those systems, leading to a situation in which the observational data is affected by undesirable degeneracies, like the widely mentioned one between age and metallicity (e.g. O’Connell 1976; Aaronson et al. 1978, Worthey 1994a). The most widely used technique to compare galaxies with models is to measure certain line strength indices, on the

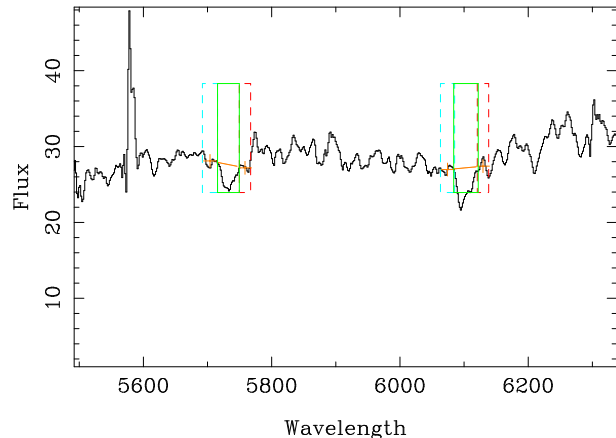


Figure 7. Example of the method used to derive the H β and Mgb line indices. The plot shows a detail of the spectrum of the galaxy number 2 (IFU_{id}), zoomed in onto the region of interest. For each absorption line the boxes indicate the regions where the adjacent continuum are estimated (blue and red boxes) together with the region where the absorption is measured. The orange line indicates the adopted slope for the continuum. The strong feature at 5577Å is the residual of the non perfect subtraction of a night sky emission line.

Lick/IDS index system (Burstein et al. 1984; Faber et al. 1985; Burstein, Faber & González 1986; Gorgas et al. 1993; Worthey et al. 1994). People generally try to use a combination of indices that are most orthogonal in parameter space (e.g. age and metallicity; although see Cardiel et al. 2003 for a discussion of the impact of random errors in the selection of the best combination of indices). Following the Lick/IDS definitions, for our study we have chosen H β as a primary age indicator, and the Mgb index as a metallicity indicator. We use the Mgb index rather than the more conventional [MgFe] one, because both we and Ziegler et al. (2001) are unable to derive reliable Fe indices for most of the galaxies. This diagram has the drawback that the models based on solar abundance ratios do not match the Mg/Fe ratio observed in early-type galaxies (Thomas et al. 1999, 2004). It is also well known that the ages derived from the grid are clearly uncertain in an absolute sense. However, we are primarily interested in a relative comparison of the ages and metallicities of the galaxies in the cluster, and in this sense the diagram is valid.

As we will discuss below, a proper estimate of those indices requires high signal-to-noise spectra, and may be strongly affected by the instrumental and systemic velocity dispersions, the presence of weak emission lines that fill the absorptions (specially important in the case of H β), and the presence of high residuals corresponding to the removal of nearby sky emission lines.

3.7.1 Analysis of line-strength indices

We derive the H β and Mgb equivalent widths for our IFU sample using the bandpass definitions from the Lick index system revised by Trager et al. (1998), shifted to the redshift of each object. We used our own routines and checked

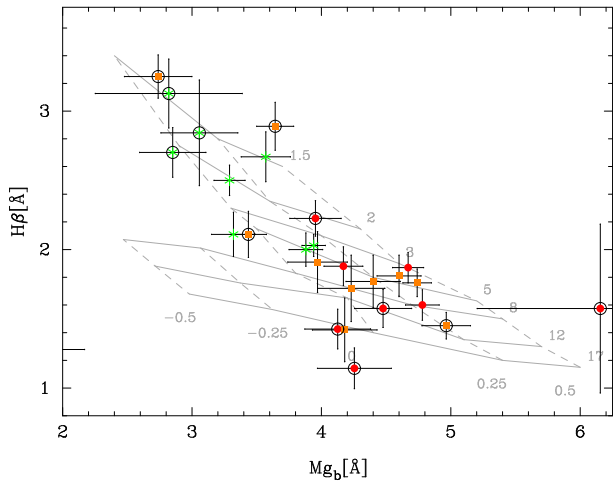


Figure 8. Age - metallicity diagnostic diagram using $H\beta$ as a primary age indicator and Mg_b as a metallicity indicator. The symbols are similar to those ones in Fig.6. Overplotted is a grid of SSP models from Worthey (1994b). ‘Horizontal’ lines follow constant age (Gyr), ‘vertical’ lines constant metallicity ($[M/H]$). Each line is labeled with its corresponding age/metallicity.

the results with indexf^2 . Figure 7 illustrates the procedure, showing a detail of the spectrum of galaxy number 2 and the actual bandwidths used to derive each of the indices. The derived results are listed in Table 4, together with the error estimates (computed as explained below). We only list the positive values, since a negative equivalent width means emission, and not absorption. In most of the cases these negative values are found in faint targets, and are simply due to low signal-to-noise of the spectra. However, in a few cases they indicate real emission lines, like the strong emission lines of galaxy number 38 (the merger) or fainter ones, like in galaxies numbers 18 and 22. In these three cases it is possible to derive reliable Mg_b indices, but unreliable $H\beta$ ones. On the other hand, there are a few objects (16, 20, 21 and 25), with too low Mg_b equivalent widths for their $H\beta$ ones. A visual inspection of their spectra, and a trace back to the raw data shows that they show cross-talk contamination from ThAr emission lines obtained in adjacent calibration fibers, which unfortunately lies in the regime of the Mg_b absorption. For other four galaxies (number 1, 7, 8 and 15) both $H\beta$ and Mg_b seem to be too low. Galaxy number 1 is the cD, a kind of galaxy with well known deviations of the metallicity sensitive indices (e.g. Cardiel et al. 1998). A visual inspection of its spectrum in the $H\beta$ region indicates possible emission that fill the absorption. A similar inspection of the spectra of galaxies number 7 and 8 shows clear contaminations of sky emission line residuals in the adjacent regions to the $H\beta$ absorption band. Finally, galaxy number 15 has an uncertain redshift determination, which strongly affects the derived indices. All these objects have been excluded from further analysis based on line indices. Of the 6 galaxies in common with Ziegler et al. (2001), 5 have line-strength indices in common. In both cases, the strengths of $H\beta$ and Mg_b agree within $\pm 0.6\text{\AA}$, which is far beyond the estimated errors of both studies. However such

differences are expected on the basis of the different methods used to derive the strength of the line indices that may strongly affect the results.

We estimated the errors using Monte Carlo simulations of each spectrum, in the following way: first we derive for each spectrum the best matched single stellar population model, as we will describe in the next section. This model is included in Fig. A1. Then, we subtract the model from the spectrum, and derive the absolute value of the difference for each wavelength. Finally, we smooth this *residual* spectrum with a 10 pixels width median-box filtering. This smoothing was performed to reproduce as much as possible the noise cross-correlation pattern between adjacent pixels. The width was selected to match the spectral resolution, since we consider that this is the range of pixels where the cross-correlation of the noise is stronger. We consider that this rather complex method to estimate the errors is a better representation of the variance than the much simpler approach that would be to create a variance spectrum based on the estimated accuracy of our spectrophotometry (Sec. 2.1 and Appendix B). The reason for that is that using this latter approach we would not take local effects in the variance, like imperfections in the sky subtraction, cross-talk contaminations and unaccuracies on the reduction process. Using the adopted *variance* and our original spectrum we created 100 simulated spectra. The standard-deviation of the resulting equivalent widths are assumed to be the errors of our measurements. Line indices, for galaxies with velocity dispersions larger than 200 Km/s (derived from the fitting to SSP models, as described below), are finally corrected as in Jablonka, Gorgas and Goudfrooij (2002) by using similar coefficients (Jablonka, private communication).

The final useful dataset comprises line indices for 26 objects, 12 of them corresponding to our IFU sample. Figure 8 shows the Age - metallicity diagnostic diagram using $H\beta$ as a primary age indicator and Mg_b as a metallicity indicator. The symbols are similar to those in Fig.6, including both our determined equivalent widths and those obtained by Ziegler et al. (2001). Overplotted is a grid of SSP models from Worthey (1994b). ‘Horizontal’ lines follow constant age, ‘vertical’ lines constant metallicity. Even though there are in the literature more recent evolutionary synthesis model predictions suitable for our purposes (e.g. Bruzual & Charlot 2003, Vazdekis et al. 2003, Thomas, Maraston & Kron 2004), here we are using the classical Worthey (1994b) models because we are just interested in a differential analysis of our data (i.e. the absolute derived ages and metallicities should not be taken literally) and we can perform a direct comparison with the results published by Ziegler et al. (2001). Ziegler et al. (2001) already noticed that E-type galaxies in this cluster cover a wide range of parameters within Fig 8, much wider than similar samples in the local universe (e.g. Kuntschner et al. 2001). We confirm this conclusion, since the new galaxies have increased the range of covered parameters. The bulk of the galaxies show lower metallicities and younger ages at a fixed metallicity compared to the ones in the local universe. They suggested that these differences may be due to variations in the average masses of the two galaxy samples, in the sense that more massive galaxies tend to be older.

The Ziegler et al. (2001) sample lacks enough L-type galaxies to draw a clear conclusion on the dependence of

² <http://www.ucm.es/info/Astrof/software/indexf/>

these parameters on the morphology. With the new sample it is possible to see that L-type galaxies are found towards younger ages, on average, than E-type galaxies at any fixed metallicity. On the other hand they seem to cover the same range of metallicities at any fixed age. These conclusions have to be taken with care, since most of our L-type galaxies are, at the same time, less luminous and therefore less massive than our E-type ones (Fig. 6). Therefore, if there is a correlation between the age and the mass, as suggested by Ziegler et al. (2001), this trend may affect both the E-type and the L-type galaxies, and explain our results. We will further investigate this possibility below.

3.7.2 Fitting to Single Stellar Population models

Cardiel et al. (2003) already showed how sensitive the derivation of physical parameters from line indices is to the signal-to-noise of the spectra. They concluded that using the full spectrum, when possible, one can derive better parameters, for a similar signal-to-noise. In the previous section we have seen that even for high signal-to-noise spectra local contaminations from emission lines, both from the object and/or residuals from the sky or cross-talk from calibration fibers can strongly affect the derived indices.

To extract the maximum information for the maximum number of objects we fitted each spectrum from our IFU sample with synthetic SSP models. Models were created using the GISSEL code (Bruzual & Charlot 2003), assuming a Salpeter (1955) IMF (the use of a Chabrier (2003) will not modify the results), for different ages and metallicities. We create 72 models covering a discrete grid of 12 ages (5 Myr, 25 Myr, 100 Myr, 290 Myr, 640 Myr, 0.9 Gyr, 1.4 Gyr, 2.5 Gyr, 5 Gyr, 11 Gyr, 13 Gyr, and 17 Gyr), and 6 metallicities ($Z = 0.0001, 0.0004, 0.004, 0.008, 0.02$ and 0.05). Each spectrum was then fitted to each of the 72 models using FIT3D (Sánchez et al. 2006b). This code resamples the model to the resolution of the data, convolve it with a certain velocity dispersion, shift it to the redshift of the target and scale it to match the dataset by a χ^2/ν minimization scheme. Therefore, for each SSP model, these are the three free parameters in the fitting process: velocity dispersion, redshift and a scaling factor related to the luminosity. The redshift of the object was fixed to reduce the degrees of freedom. Only the spectral region at wavelengths bluer than 7200 Å was used in this analysis. At redder wavelengths the strong night sky emission-lines and the telluric absorptions have not properly been corrected for in our reduction process, and strong residuals are seen in the spectra. Wavelength regions possibly affected by imperfect sky emission line subtraction were also masked. We derived the velocity dispersions for each object spectrum in the fitting process, including both the intrinsic and instrumental ones. We cannot perform an accurate correction of the instrumental effects cause we lack of the proper comparison observations of velocity calibration stars during the night. This prevents us to use them as a mass indicator (e.g. Ziegler et al. 2001), using them only to correct the line-indices strength, when required. The corrected velocity dispersions range between ~ 100 -400 km s⁻¹, and despite the lack of accuracy of our derived velocity dispersions they agree with the ones derived by Ziegler et al. (2001), for the 6 objects in common.

We obtain for each spectrum a grid of 72 χ^2/ν , each

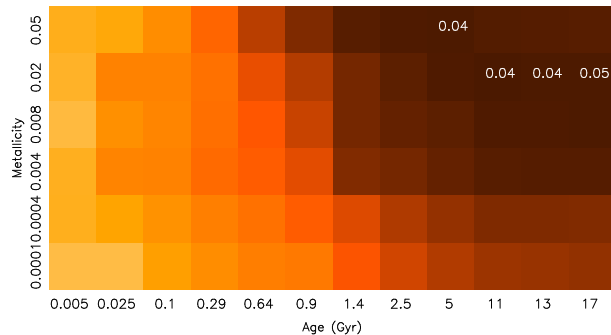


Figure 9. Greyscale image of the 2D distribution of χ^2/ν derived from the fitting of a single galaxy spectrum to a grid of SSP models of different ages and metallicities. Dark colors indicate lower χ^2/ν (i.e., better fits), while light colors indicate higher values (i.e., worse fits). The χ^2/ν of the four best fits are labeled. The plotted example corresponds to the second brightest galaxy in our field-of-view (id=2 in Table 4)

one corresponding to an age-metallicity pair model. Figure 9 illustrates the result of the fitting technique. It shows a greyscale of the χ^2/ν map derived after fitting the spectrum of galaxy number 2 to the grid of models, each one corresponding to an age-metallicity pair. Similar results are found for the rest of the objects. In the fitting procedure we assumed a simple root-mean-square of the flux as an estimation of the uncertainties in the spectra, to derive the χ^2/ν . Therefore these values are not valid to compare the results of the fit for different objects, and just to perform internal comparisons between the results of the fit for the same object. The χ^2/ν of the four best fits are indicated in the figure. In general it is not possible to distinguish which is the best fitting model among the best four ones. Therefore, we estimate the age and metallicity of each object by averaging the ages and metallicities of the four best models, weighted by the inverse of the corresponding χ^2/ν values. Errors for the estimated parameters are derived by Monte Carlo simulations: for each spectrum we estimate the *variance* spectrum as described above. Then we created 30 simulated spectra, using as input the original spectrum and adding noise following the estimated *variance*. For each of the 30 simulated spectra we run the fitting process over the 72 models (i.e., 2160 fits per input spectrum), and the age and metallicity are derived following the recipe described above. The standard deviation of the recovered distribution of ages and metallicities for the simulated spectra is considered as a good estimate of the error of the measured parameters for the input spectrum. The final errors for the ages and metallicities are computed coadding quadratically these estimated errors to the standard deviation of the values for the four best models. The results from this procedure are listed in Table 4.

The method relies on certain assumptions: (i) we consider that the use of the full spectrum is a better method to recover the age and the metallicity of the main stellar population than just using the line indices and (ii) we consider that our spectrophotometric calibration is stable from blue-to-red, i.e., that the shape of the spectra is well recovered. This is a sensitive assumption, since the whole method relies on it. To test its validity we compared our integrated spectra with the available broad-band photometry (Fig. A1).

The photometric dataset, derived from the HST/ACS data, covers the full optical wavelength range, from $\sim 4700\text{\AA}$ to $\sim 9000\text{\AA}$, and in particular the wavelength range of our spectroscopic data. In most of the cases our spectroscopic data match pretty well with the broad-band photometric ones. Even more, the extrapolation of the data using the best fitted SSP synthetic model reproduces also the expected photometry in wavelength ranges not covered by our spectroscopic data in most of the cases. Only galaxies number 9, 11, 16, 18, 22 and 24 show a slight mismatch ($\sim 2\sigma$) between the extrapolated flux and the z_{850} -band photometry. If we take into account that the spectrophotometry seems to match for the rest of the bands and for the rest of the objects, we have strong arguments to consider that is also valid for these ones: We used an IFU, and therefore the flux calibration was performed only once for the full dataset.

Finally we assume that (iii) the adopted grid of models comprises a good representation of the expected stellar populations. We tried not to pre-judge the composition of the stellar population and cover the wider possible range of ages and metallicities. On the other hand, we must limit the number of input models for a reasonable performance of the fitting procedure. This imposes limitations on the sampling of the grid, and therefore, in the accuracy of the recovered age and metallicities. We must take that into account when drawing conclusions from our modelling.

3.7.3 The Age-Metallicity Distribution

Figure 10 shows the distribution of the metallicities as a function of age derived using the previously described fitting procedure for the galaxies in our IFU sample. The symbols are similar to the ones in Fig.6. The size of the symbols indicates the mass (see below for a description of how it was estimated), with larger symbols for more massive objects. The merging galaxy (IFU_{id} = 38), is not visible in this plot, since the derived age for its stellar population, $\sim 250\text{Myr}$, is far from the average of the rest of the sample. This result is expected due its $B - V$ color, and the strong star formation process that is derived from the strength of the emission lines on its spectrum. In this particular case a SSP model is not a good enough to describe the expected mix of populations resulting from a merging process, with at least an underlying stellar population, and a younger one resulting from the induced star formation process.

If we compare this figure with the $H\beta$ - Mgb distribution shown in Fig. 8 evident differences can be seen. However, a direct comparison has to be done with care. First, the absolute ages and metallicities derived from both figures cannot be compared, since they come from completely different SSP models. We used the Worthey (1994b) models in the previous figure to be consistent with Ziegler et al. (2001), while the models used in the fitting procedure are derived from the GISSEL code (Bruzual & Charlot 2003). However, relative comparisons between the different galaxies are possible, in principle. One needs to take into account that in Fig.8 we only represent 12 of the 27 objects shown in the current plot, i.e., mostly the brightest ones. On the other hand, the objects from Ziegler et al. (2001) are not plotted in the current figure. However, the conclusions about the stellar populations of individual galaxies derived from both figures agree qualitatively: the galaxies with young and old

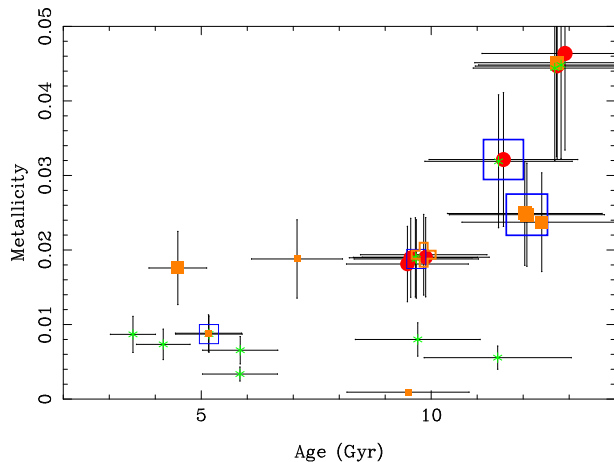


Figure 10. Distribution of the metallicities as a function of age derived by the fitting procedure for the 28 galaxies our IFU sample. The symbols are similar to those ones in Fig.6. The size of the symbols indicate the mass, with larger symbols for more massive objects. All the E-type galaxies ($n > 2.5$), and most of the $n > 1.75$ ones have stellar populations older than ~ 9 Gyr and a wide range of metallicities, $0.02 < Z < 0.05$.

stellar populations have young and old stellar populations in both figures, and the galaxies richer and poorer in metals are richer and poorer in both figures too.

We consider the current figure a more accurate representation of the real distribution of ages and metallicities of the galaxies in the cluster (or at least in the core). The plotted parameters were derived for the IFU sample, which is complete to our detection limit, without any pre-selection and any *a posteriori* exclusion. In general it is found that the galaxies with older stellar populations covers a wider range in metallicities, being more metal rich, on average, than the galaxies with younger stellar populations. This result does not agree with the trend between these two parameter found in field ellipticals, where galaxies with younger stellar populations are more metal rich (e.g. Trager et al. 2000). However, our sample comprises a large fraction of L-type galaxies. As in Fig 6 we found a clear different behaviour for the E-type and L-type galaxies. All the E-type galaxies with $n > 2.5$ (spheroidals), and most of the $n > 1.75$ ones (intermediate galaxies) have stellar populations older than ~ 9 Gyr, covering a wide range of metallicities, $0.02 < Z < 0.05$. On the other hand, the L-type galaxies ($n < 1.75$), cover a much wider range of ages, from ~ 3 Gyr to ~ 13 Gyr (keeping in mind that the absolute ages have no meaning), and metallicities, $0.001 < Z < 0.05$. Interestingly, the L-type galaxies with the largest metallicities ($Z > 0.015$) seems to have similar ages as the E-type ones, and the L-type galaxies with smaller metallicities cover a wider range of ages. The most metal rich galaxies are the more massive ones (with larger symbols), and therefore, this result may indicate that more massive galaxies tend to be older whatever their morphologies. We will discuss that in detail below. This result is certainly not clear from Fig.8.

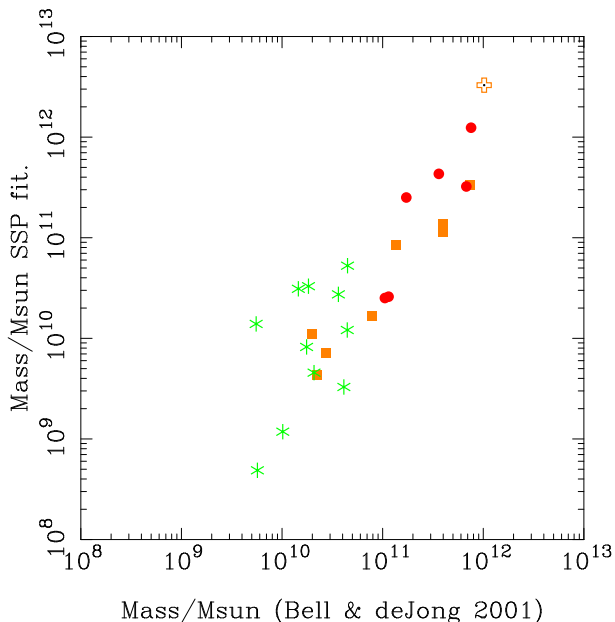


Figure 11. Distribution of the stellar masses for the galaxies of our sample derived from the results of the fitting procedure to SSP models along the stellar masses derived using the Bell & de Jong (2001) approximation.

3.8 Stellar populations and Masses of the Galaxies

In previous sections we have already seen that the masses of the galaxies are directly related to the nature of their stellar populations. The Color-Magnitude diagram, Fig. 6, shows that less luminous (and massive) galaxies show a wider range of colors than more luminous objects. The comparison of the $H\beta$ - Mgb distribution of this cluster with that of the local universe, including more massive galaxies, makes Ziegler et al. (2001) think that there might be a trend of metallicities/ages with the mass of the objects. Figure 10 shows that more massive galaxies are, on average, older and more metal rich. We investigate here the possible relations between the stellar populations and the morphology with the mass of the galaxies.

It is well known that the masses of spheroidal or early-type galaxies are directly related to their stellar velocity dispersions (σ), due to their nature. This parameter, directly accessible from the spectra, has indeed been used as a mass indicator for decades, leading to a set of well established scaling relations when comparing it with different properties of the galaxies. Among these relations the most important ones are the luminosity-velocity dispersion relation or Faber-Jackson relation (Faber & Jackson 1976), the surface brightness, effective radius and velocity dispersion relation or Fundamental plane (Dressler et al. 1987; Djorgovski & Davis 1987; Bender et al. 1992) and the Mg -velocity dispersion relation or Mgb - σ relation (Bender et al. 1993; Colless et al. 1999). These scaling relations have been used to compare between different populations of early-type galaxies at different redshifts (e.g. Ziegler et al. 2001), to trace the evolution of this kind of galaxies. For late-type galaxies similar relations are found when using the maximum rotating velocity, a parameter directly related with the mass of the rotating disk.

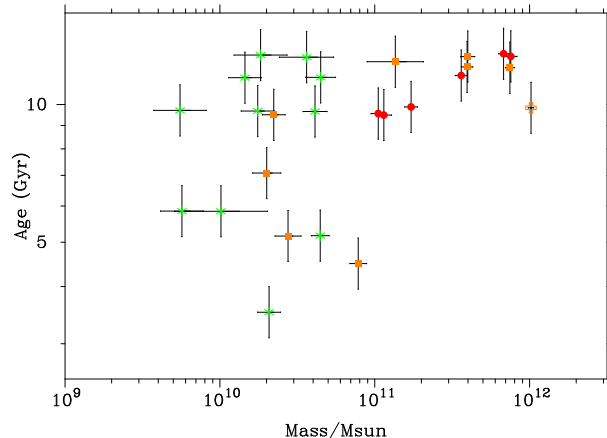


Figure 12. Distribution of ages along stellar masses for the our galaxy sample. The symbols are similar to those ones in Fig.6. There is a clear morphological segregation. L-type galaxies are less massive than $10^{11} M_{\odot}$, and have a wider range of ages than E-type galaxies.

All these relations have a direct correspondence with relations between the mass and the different properties of the galaxies: The Faber-Jackson relation can be understood as a Luminosity-Mass relation, the Fundamental plane as a Mass-scale relation and the Mg - σ as a Metallicity-Mass relation. Our spectroscopic data lack the required resolution and signal-to-noise for a proper determination of the velocity dispersion for most of the galaxies, therefore, we prefer to investigate these relations using the stellar masses of the galaxies. This approach has the advantage that we can explore at the same time all the galaxies of the sample independent of their morphology.

We estimate the stellar masses using the average relation found by Bell & de Jong (2001) between the M/L for the B -band luminosity and the $B - V$ color. For doing that we derive the rest-frame $B - V$ colors of our objects using the best fitted SSP model described before, synthesizing the magnitudes by convolving the model with the filter responses, and obtaining the B -band absolute magnitude from our photometric data. It is important to note that the masses of Bell & de Jong (2001) are just relative values, calibrated under the assumption that spiral galaxies are in a maximum-disk situation. However, this will not affect our results since we are interested in relative comparisons between different families of galaxies. The derived masses are listed in Table 4. The errors listed in the table were derived from the photometric errors in the B -band magnitudes listed in Table 2, and they do not include any other possible source of error (like the unaccuracy of the fitting process or the derived synthetic colors). However, we consider that this error dominates any other possible one. The masses of the objects range between $\sim 10^9$ and $\sim 10^{12} M_{\odot}$, being the cD galaxy the most massive galaxy and the merging galaxy the least massive one.

3.8.1 The Age-Mass relation

Figure 12 shows the age distribution as a function of stellar masses for the galaxies of our IFU sample. The symbols are similar to those in Fig.6. The division of galaxies in terms

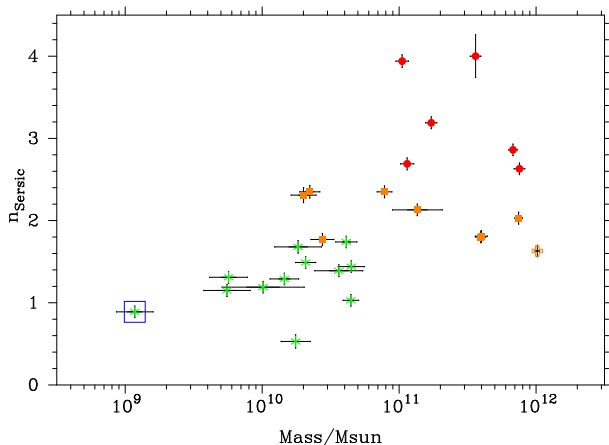


Figure 13. Distribution of Sérsic indices as a function of the stellar masses for the galaxies of our sample. The symbols are similar to those in Fig.6. There is a clear trend in the sense that E-type galaxies are more massive than L-type ones.

of morphologies is remarkably similar to that of the Color-Magnitude relation (Fig.6), although in the current plot the segregation between early- and late-type galaxies is much stronger. Most of the E-type galaxies ($n > 1.75$) and all the ones with $n > 2.5$ are more massive than $\sim 7 \cdot 10^{10} M_{\odot}$ and have stellar populations older than ~ 9 Gyr. On the other hand, all the L-type galaxies are less massive than this limit, and the ages of their stellar populations spread towards younger ages. There is no obvious trend of age with mass, but there is a lack of young stellar populations in massive galaxies. Since all of them are E-type ones, it is not possible to know if this deficit is due to the mass or the morphology of the galaxies. However such a trend it is expected, at least for field early-type galaxies. Recently Peletier et al. (2006) reported a trend between the age and the mass for field early-type galaxies based on data from the SAURON project (Bacon et al. 2001).

Figure 13 illustrates this effect. It shows the distribution of Sérsic indices as a function of the stellar masses for the galaxies of our IFU sample. The symbols are similar to those in Fig.6. There is a strong correlation between both parameters, in the sense that E-type galaxies are massive and L-type ones less massive. The relation is clearer when masking the cD and the merger galaxies, for which the profiles are not well represented by the adopted model.

Similar results were already presented by Ziegler et al. (2001) for the early-type galaxies of A2218 in the outer regions. They compared the $H\beta$ index with the stellar velocity dispersion finding that the fainter galaxies shows a larger scatter in their $H\beta$ values, indicating a wide range of star formation histories. Our survey goes deeper, sampling galaxies much fainter (and less massive) than those ones studied by Ziegler et al. (2001), extending their conclusions to fainter regimes.

3.8.2 The Metallicity-Mass relation

As we pointed out above, the $Mgb-\sigma$ relation can be understood as a metallicity-mass relation. Figure 14 shows the distribution of the metallicities as a function of the stellar mass for the galaxies of our IFU sample. The symbols are similar

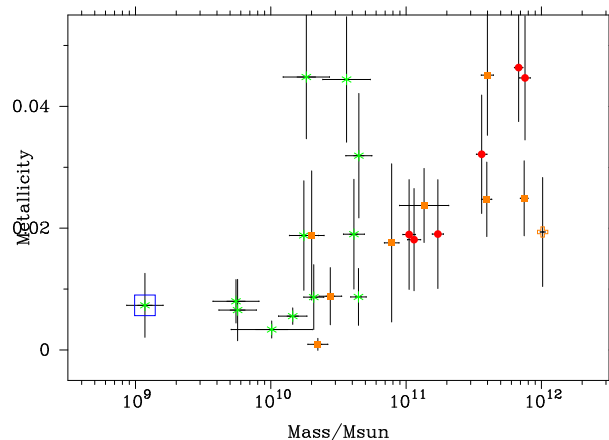


Figure 14. Distribution of the metallicities as a function of stellar mass for the galaxies of our sample. The symbols are similar to those ones in Fig.6. There is a clear correlation between both parameters, in the sense that more massive galaxies are more metal rich than less massive ones.

to those ones in Fig.6. As expected there is a clear correlation between both parameters ($r = 0.997, P > 99.99\%$), in the sense that massive galaxies of any kind are more metal rich than less massive ones. A similar result is found when using the mass derived by the fitting to SSP synthetic models, instead of the adopted one, based on the Bell & de Jong (2001) relation. Although the result is not surprising for the E-type galaxies, it is interesting that the L-type galaxies follow a similar relation, but with an offset. The trend between metallicity and mass seems to be universal for any kind of galaxy, despite of its morphology. However, for any fixed mass the L-type galaxies seem to be more metal rich than the E-type ones. This effect is not due to a difference in age of the stellar populations, since at equal age we observe a considerable range in metallicity. However, our sample is too reduced to draw firm conclusions.

4 DISCUSSION

The galaxy population of clusters in the local universe are dominated by early-type galaxies (E's and bulge-dominated spirals) Hubble & Humason (1931); Oemler (1974), with a reduced fraction of late-type galaxies (Spirals, Irregulars and Mergers). There is a general agreement about the ages of the stellar populations in early-type cluster galaxies. It is well known that they show a strong color-magnitude relation at various redshifts consistent with passive evolution of stellar populations that formed at $z > 2-3$, with a slope due to the mass-metallicity relation (e.g. Stanford et al. 1997, 1998; Kodama et al. 1998; Poggianti 2003). The spectroscopic features and the scaling relations, like the fundamental-plane, the mass-to-light ratio, the $Mgb-\sigma$ and the Faber-Jackson relations, explored at different redshift are also consistent with passive evolution of an old stellar population (e.g. Bender et al. 1996; van Dokkum & Franx 1996; Kelson et al. 2001; Ziegler et al. 2001; van Dokkum et al. 2001).

However, this apparently simple scenario for the evolution of early-type galaxies in clusters needs to be contrasted with another results. Fasano et al. (2000) show that

there is a substantial morphological evolution in clusters: as the redshift decreases the S0 population tends to grow at the expense of spiral population, whereas the frequency of spheroidals remains almost constant. Therefore the population of early-type galaxies observed in distant clusters does not necessarily comprise all the early-type galaxies existing at $z=0$ (Poggianti 2003). On the other hand, the blue galaxies observed in distant clusters, responsible of the Butcher-Oemler effect, must largely become red and fainter. There is strong evidence for a quenching of star formation in galaxies as a consequence of the infall in the cluster dense regions (Poggianti et al. 2001; Poggianti 2004), although a previous starburst may be also present (Poggianti 2004). For galaxies with a star formation history typical of L-type, once truncated, it is expected that they become redder and fade by 0.5-1.5 mag in $\sim 2-5$ Gyr (Poggianti 2004). Finally, although the spectrophotometric and the morphological evolution seems to be largely decoupled, it is expected that after longer timescales there will a morphological transformation from pure L-type to bulge-dominated spirals (Fasano et al. 2000). All these results suggest that the early-type galaxies in clusters are composed of a mix of different stellar populations, with very different origins, contrary to the simple scenario drawn above.

How do our results compare with previous knowledge of the evolution of galaxies in clusters? The morphological distribution of the cluster members derived from our analysis is: 11 (7) E-type, 19 (8) lenticulars, and 29 (13) L-type, for our complete sample (our IFU sample). In percentages it is: 19% (25%) E-type, 32% (29%) lenticulars and 49% (46%) L-type. These fractions differ strongly with the estimated ones for clusters at similar redshifts: 30% E-type, 50% lenticulars and 20% L-type (Fasano et al. 2000), showing a much larger fraction of late-type galaxies. Fasano et al. (2000) estimated these numbers based on images with limiting magnitudes of the order of $r \sim 20.2-20.5$ mag, i.e. $\sim 1.5-2$ mag less deep than our current survey (taking into account the range of possible $r - z$ colors for any kind of galaxy at this redshift, from ~ 0 mag to ~ 0.6 mag, Fukugita et al. 1995). If we consider only the objects brighter than $z < 20$ mag, the new morphological segregation is: 9 (7) E-type, 16 (7) lenticulars and 16 (4) L-type. These percentages are within the values reported by (Fasano et al. 2000): 22% (39%) E-type, 39% (39%) lenticulars and 39% (22%) L-type. Therefore, there is an increase of the fraction of late-type galaxies at fainter magnitude regimes.

Looking at Figures 6 and 12 it is possible to identify two kind of L-type galaxies in the faint magnitude regime: (i) a group of blue and faint galaxies, with young stellar populations (< 8 Gyr), and (ii) another group of red and faint galaxies, with older stellar populations (> 8 Gyr). The first ones are the kind of galaxies responsible for the Butcher-Oemler effect. Galaxies recently captured by the cluster, with relatively young stellar populations and traces of recent star formation processes. Due to their colors these galaxies would be detected in surveys in the optical/blue bands. The second group are the kind of galaxies predicted in the two-steps evolution hypothesis for galaxies captured by clusters, where the star formation was quenched first, and then there was a slower morphological transformation (Poggianti et al. 2001; Poggianti 2003). As a first step the late-type galaxies fall into the cluster, and due to gas stripping the star for-

mation process is abruptly interrupted (maybe after a short starburst process). Then, these galaxies become fainter and redder, while still showing a spiral shape.

Clusters with the highest fraction of blue galaxies shows signs of recent mergers, and there are larger fractions of star-forming galaxies in substructured than in relaxed clusters (e.g. Smail et al. 1998; Metevier et al. 2000; Pimblet et al. 2002). Theoretical simulations predict that the cluster mergers induces a starburst processes, due to the strong tidal forces involved (e.g. Moss & Whittle 2000), a similar effect of galaxy-galaxy interactions (e.g. Mihos & Hernquist 1996). Abell 2218 shows two clear peaks in the X-ray and galaxies distribution (McHardy et al. 1990), indicating that it most probably has suffered a recent (or ongoing) merging. This may account for the moderate Butcher-Oemler fraction of blue galaxies quoted in classical studies ($\sim 10\%$ Butcher & Oemler 1984).

Galaxies captured by the cluster may suffer similar tidal forces, which may induce an enhancement of the star formation process, previous to the quenching due to gas stripping (Poggianti 2003). The location of the k+a (post-starburst) galaxies, and the strength of their Balmer absorption features strongly supports this hypothesis (Poggianti 2004). To our knowledge, Abell 2218 is the only cluster at cosmological distances where HI is observed in emission (Zwaan et al. 2001), at the location of a spiral galaxy in the outer regions of the cluster. This galaxy is most probably an infalling spiral, consuming its gas reservoir with ongoing star formation (estimated SFR of $< 1.4 M_{\odot}/\text{yr}$). More spectacular is galaxy number 38 from our IFU sample, a blue disrupted galaxy at the nominal redshift of the cluster with a very little projected distance from the center of the cluster. It is possible that this galaxy has been recently captured by the cluster, and that it is moving in an orbit perpendicular to the line-of-sight. If not, there should be a conspiracy between its cosmological redshift and line-of-sight velocity to compensate each other so that it appears to be at the nominal redshift of the cluster, which is an unlikely explanation. Its emission lines indicate a moderate amount of ongoing star formation, with a $\text{SFR} \sim 6 M_{\odot}/\text{yr}$, derived from the $\text{H}\alpha$ emission (Kennicutt 1983; Kennicutt et al. 1994). No dust is derived from the $\text{H}\alpha/\text{H}\beta \sim$ ratio, ~ 2.9 , nearly the nominal value for case B recombination. Its dominant stellar population has an age of ~ 250 Myr, which could be a feasible time-scale for the infall process. Its morphology is similar to that one of a merger in its last stage, however, the strong tidal forces that may suffer during the infalling process may have produce the same effect. If the proposed scenario for the evolution of galaxies in cluster is true, this galaxy would be a good candidate for a progenitor of the observed k+a galaxies at low-redshift (Poggianti 2004). In a recent study of Abell 2125, a dense cluster at $z \sim 0.247$, Owen et al. (2006) found a galaxy with strong emission lines (maybe even with an AGN), blue colors, and a disturbed morphology. Although that galaxy is brighter than galaxy number 38, both systems seem to experience the same physical process.

Our results indicate that there is a correlation between the morphology and the mass, in the sense that less-massive galaxies are mostly L-type and more-massive ones are mostly E-type (Fig. 13). This result is natural in the proposed scenario, where the morphological transformation between L-type to bulge-dominated spirals, and later to E-type galax-

ies is a consequence of consecutive merging processes. We have also found a clear correlation between the mass and the metallicity, in the sense that more massive galaxies are more metal rich (Fig. 14). This correlation is an extension of the well known Mg- σ relation for spheroidal galaxies, which seems to be independent of the galaxy morphology. Although we have a very reduced sample, it seems that L-type galaxies are more metal-rich than E-type ones at any fixed mass. Figure 14 also indicates that the more metal rich L-type galaxies are never more metal than the E-type ones, being only less massive. To our knowledge this effect has not been previously reported in the literature, and it may well be an effect of the very reduced sample. If not, it may imply that the galaxies reach their maximum metallicity when they are still spirals, maybe due to the enhancement of the star formation rate when infalling into the cluster, and that they later evolve to more massive bulge-dominated spirals and E-type galaxies keeping this metallicity.

5 CONCLUSIONS

We obtained deep IFS data ($I_{lim} \sim 21.4$ mag) covering a field-of-view of $\sim 74'' \times 64''$ centred on the core of the galaxy cluster Abell 2218, sampling the wavelength range 4650-8000Å with a resolution of $\sim 10\text{Å}$ (FWHM). Combining these data with a deep HST/ACS F850LP-band image ($z_{lim} \sim 28$ mag), and ground-based and HST/WFPC photometric data, we have obtained the following results:

- Morphological parameters of all the galaxies in the field-of-view of the HST/ACS image down to $z < 22.5$ mag were obtained, based on an automatic procedure using `galfit`.
- The integrated spectrum of each of the 43 objects detected in the IFU datacube was obtained, using a modeling technique for IFS (`galfit3d`), which ensures a proper deblending of multiple components in crowded-fields.
- Of the detected objects, 28 were classified as cluster members based on their redshifts. They comprise the first volume and flux limited sample of confirmed cluster members obtained for the core of this cluster. We need to remark that the sample was obtained without any pre-selection based on morphology, colors or magnitudes.
- By combining the different previous redshift and photometric surveys with our new morphological information an extended sample of 59 cluster members was created, 31 of them sampling the outer regions of the cluster (out of the core).
- The color-magnitude diagram of the full sample of confirmed cluster members, as a function of the morphology, was analyzed. We have found that the fraction of early-type galaxies is lower than previously reported, most of them being red and luminous galaxies. On the other hand, the L-type galaxies spread over a wider range of colors and luminosities with respect to the E-type ones and previously published catalogs.
- There is no significant difference between the Color-Magnitude distributions of the galaxies in the core of the cluster and in the outer regions if one distinguishes between different morphologies. If any, we found a few more L-type faint and red galaxies in the core. However, this may be due to the biases of the pre-selection of candidates in the samples obtained from the literature (in the outer regions).

- A strongly distorted blue galaxy is found in projection at the core of the galaxy cluster. Its redshift corresponds to the nominal redshift of the cluster, and therefore, it is more likely that it is physically located in the core. A visual inspection of the object indicates that it looks like a merger in an advance stage of evolution, dominated by a young stellar population. However, if we are observing it in the moment of being captured by the cluster, the strong tidal forces that it is suffering may produce the observed disruption on its morphology.

- The analysis of the age and metallicity of a reduced subsample of galaxies (24 galaxies, 12 core members) based on line indices indicates that L-type galaxies on average spread towards younger ages than E-type ones. On the other hand, they seem to cover the same range of metallicities at any fixed age.

- The age and metallicity of each galaxies in the core of the cluster was derived by a fitting procedure of its integrated spectrum to single stellar population models. The age-metallicity diagram of these galaxies indicates too that L-type galaxies cover a clearly wider range of ages, and a slightly wider range of metallicities. The more massive L-type galaxies seem to have similar ages and metallicities than the E-type ones, while the less massive ones tend to be younger and less metal rich.

- The distribution of ages and Sérsic indices as a function of the stellar masses of the core members shows that L-type galaxies are less massive on average. They spread over a wider range of ages, but it is not possible to determine if this is due to their morphologies or masses. On the other hand, more massive galaxies tend to have older stellar populations and they are all early-type galaxies.

- There is a clear trend between the metallicity and the mass, in the sense that more massive galaxies are more metal rich. This trend is just a change of coordinates of the well known Mgb- σ relation for the early-type galaxies. However, we found that this trend is also present for the L-type galaxies, but with an offset: they are more metal rich than E-type galaxies at any fixed mass.

Our results agree with the proposed two-steps scenario for the evolution of galaxies in clusters (e.g. Poggianti 2003), in which we have (i) a primordial population of early-type galaxies formed at early epochs with stellar populations that are mostly old, and (ii) a new population of L-type galaxies that are captured by the cluster, infalling, suffering a short enhancement of the star formation that is later quenched by the interaction with the environment. The galaxies then evolve passively, becoming redder and fainter, while keeping the spiral morphology. The disks dim due to the lack of new formed stars, and the galaxies become bulge-dominated spirals, after longer time-scales. Later galaxy-galaxy interactions and dry merging processes build up new massive spheroidal galaxies.

ACKNOWLEDGMENTS

Based on observations collected at the Centro Astronómico Hispano Alemán (CAHA) at Calar Alto, operated jointly by the Max-Planck Institut für Astronomie and the Instituto de Astrofísica de Andalucía (CSIC) Based in part on observations with the NASA/ESA *Hubble Space Telescope*,

obtained at the Space Telescope Science Institute, which is operated by the Association of Universities for Research in Astronomy, Inc., under NASA contract NAS 5-26555.

We thank Dr. R. Gredel, former director of Calar Alto, for supporting this work and providing us with the telescope time for finishing it.

We thank support from the Spanish Plan Nacional de Astronomía program AYA2005-09413-C02-02, of the Spanish Ministry of Education and Science and the Plan Andaluz de Investigación de Junta de Andalucía as research group FQM322.

We thank Dr. R. Peletier, who kindly read the article cleaning the English. His comments on the science content have helped us to increase the quality of this article.

REFERENCES

- Abell, G. O., Corwin, H. G., & Olowin, R. P. 1989, *ApJS*, 70, 1
- Andredakis, Y. C., Peletier, R. F., & Balcells, M. 1995, *MNRAS*, 275, 874
- Andreon, S. 1998, *ApJ*, 501, 533
- Aragon-Salamanca, A., Ellis, R. S., Couch, W. J., & Carter, D. 1993, *MNRAS*, 262, 764
- Aaronson M., Cohen J.G., Mould J.R., Malkan M., 1978, *ApJ*, 223, 824
- Balogh M.L., Morris S.L., Yee H.K.C., Carlberg R.G., Ellingson E., 1999, *ApJ*, 527, 54
- Bacon, R., et al. 2001, *MNRAS*, 326, 23
- Barazza, F. D., Binggeli, B., & Jerjen, H. 2003, *A&A*, 407, 121
- Barazza, F. D., et al. 2006, *ApJ*, 643, 162
- Bell, E. F., & de Jong, R. S. 2001, *ApJ*, 550, 212
- Bell, E. F., McIntosh, D. H., Barden, M., Wolf, C., Caldwell, J. A. R., Rix, H., Beckwith, S. V. W., Borch, A., Häussler, B., Jahnke, K., Jogee, S., Meisenheimer, K., Peng, C., Sánchez, S. F., Somerville, R. S., & Wisotzki, L. 2004, *ApJL*, 600, L11
- Bell, E. F., et al. 2006, *ApJ*, 640, 241
- Bender, R., Burstein, D., & Faber, S. M. 1992, *ApJ*, 399, 462
- Bender, R., Burstein, D., & Faber, S. M. 1993, *ApJ*, 411, 153
- Bender et al. 1996, *ApJ*, 463, L51
- Bertin, E., & Arnouts, S., 1996, *AAS*, 117, 393
- Bruzual, G., & Charlot, S., 2003, *MNRAS*, 344, 1000
- Burstein D., Faber S.M., Gaskell C.M., Krumm N., 1984, *ApJ*, 287, 586
- Burstein D., Faber S.M., González J.J., 1986, *AJ*, 91, 1130
- Butcher, H., & Oemler, A. 1978, *ApJ*, 219, 18
- Butcher, H., & Oemler, A. 1978, *ApJ*, 226, 559
- Butcher, H., Wells, D. C., & Oemler, A. 1983, *ApJS*, 52, 183
- Butcher, H., Oemler, A., 1984, *ApJ*, 285, 426
- Cairós, L. M., Vílchez, J. M., González Pérez, J. N., Iglesias-Páramo, J., & Caon, N. 2001, *ApJS*, 133, 321
- Cardiel N., Gorgas J., Aragón-Salamanca A., 1998, *MNRAS*, 298, 977
- Cardiel, N., Gorgas, J., Sánchez-Blázquez, P., Cenarro, A. J., Pedraz, S., Bruzual, G., & Klement, J. 2003, *A&A*, 409, 511
- Chabrier, G. 2003, *PASP*, 115, 763
- Coe, D., Benitez, N., Sánchez, S.F., et al., 2006, *AJ*, 132, 926
- Colless, M., Burstein, D., Davies, R. L., McMahan, R. K., Saglia, R. P., & Wegner, G. 1999, *MNRAS*, 303, 813
- Conselice, C. J., Bershad, M. A., Dickinson, M., & Papovich, C. 2003, *AJ*, 126, 1183
- Couch, W. J., & Sharples, R. M. 1987, *MNRAS*, 229, 423
- Couch, W. J., Ellis, R. S., Sharples, R. M., & Smail, I. 1994, *ApJ*, 430, 121
- Covone G., Kneib, J.-P., Soucail G., Richard, J., Jullo, E., Ebeling, H., 2006, *A&A*, 456, 409
- de Vaucouleurs, G., de Vaucouleurs, A., & Corwin, J. R. 1976, Second reference catalogue of bright galaxies, 1976, Austin: University of Texas Press., 0
- Djorgovski, S., & Davis, M. 1987, *ApJ*, 313, 59
- Dressler, A., & Gunn, J. E. 1983, *ApJ*, 270, 7
- Dressler, A., Lynden-Bell, D., Burstein, D., Davies, R. L., Faber, S. M., Terlevich, R., & Wegner, G. 1987, *ApJ*, 313, 42
- Dressler, A., Oemler, A. J., Butcher, H. R., & Gunn, J. E. 1994, *ApJ*, 430, 107
- Dressler, A., et al. 1997, *ApJ*, 490, 577
- Dressler, A., et al. 1999, *ApJS*, 122, 51
- Faber, S. M., & Jackson, R. E. 1976, *ApJ*, 204, 668
- Faber S.M., Friel E.D., Burstein d., Gaskell C.M., 1985, *ApJS*, 57, 711
- Fabricant, D., Franx, M., & van Dokkum, P. 2000, *ApJ*, 539, 577
- Fasano, G., Poggianti, B. M., Couch, W. J., Bettoni, D., Kjærgaard, P., & Moles, M. 2000, *ApJ*, 542, 673
- Fritz A., Ziegler B.L., Bower R.G., Smail I., Davies R.L., 2005, *MNRAS*, 358, 233
- Fukugita, M., Shimasaku, K., & Ichikawa, T. 1995, *PASP*, 107, 945
- Gorgas J., Faber S.M., Burstein D., González J.J., Courteau S., Prosser C., 1993, *ApJS*, 86, 153
- Johnson, H. L., & Morgan, W. W. 1953, *ApJ*, 117, 313
- Hubble, E. P. 1926, *ApJ*, 64, 321
- Hubble, E., & Humason, M. L. 1931, *ApJ*, 74, 43
- Jablonka, P., Gorgas, J., Goudfrooij, P., *Astrophysics and Space Science*, 281, 367
- Kelson et al. 2000, *ApJ*, 531, 137
- Kelson et al. 2001, *ApJ*, 552, L17
- Kelz, A., Verheijen, M.A.W., Roth, M.M. et al., 2006, *PASP*, 118, 129
- Kennicutt, R. C. 1983, *ApJ*, 272, 54
- Kennicutt, R. C., Tamblyn, P., & Congdon, C. E. 1994, *ApJ*, 435, 22
- Kodama et al. 1998, *A&A*, 334, 99
- Kristian, J., Sandage, A., & Westphal, J.A., 1978, *ApJ*, 221, 383
- Kuntschner, H., Lucey, J. R., Smith, R. J., Hudson, M. J., & Davies, R. L. 2001, *MNRAS*, 323, 615
- Le Borgne, J.F., Pelló, R., Sanahuja, B., 1992, *A&AS*, 85, 87
- García-Lorenzo, B., Sánchez S.F., Mediavilla, E., et al., *ApJ*, 621, 146
- McHardy, I.M., Stewart, G.C., Edge, A.C., et al. 1990, *MNRAS*, 242, 215
- Metevier, A. J., Romer, A. K., & Ulmer, M. P. 2000, *AJ*, 119, 1090

- Mihos, J. C. & Hernquist, L. 1996, *ApJ*, 464, 641
- Moore, B., Katz, N., Lake, G., Dressler, A., & Oemler, A., Jr. 1996, *Nature*, 379, 613
- Moss, C., & Whittle, M. 2000, *MNRAS*, 317, 667
- O'Connell R.W., 1976, *ApJ*, 206, 370
- Oemler, A. J. 1974, *ApJ*, 194, 1
- Oemler, A., Jr. 1976, *ApJ*, 209, 693
- Owen, F. N., Keel, W. C., Wang, Q. D., Ledlow, M. J., & Morrison, G. E. 2006, *AJ*, 131, 1974
- Peng, C.Y., Ho, L.C., Impey, C.D., Rix, H., 2002, *AJ*, 124, 266
- Peletier, R., 2006, *MNRAS*, in preparation
- Pimblet, K. A., Smail, I., Kodama, T., Couch, W. J., Edge, A. C., Zabludoff, A. I., & O'Hely, E. 2002, *MNRAS*, 331, 333
- Poggianti, B. M., Smail, I., Dressler, A., Couch, W. J., Barger, A. J., Butcher, H., Ellis, R. S., & Oemler, A. J. 1999, *ApJ*, 518, 576
- Poggianti, B. M., et al. 2001, *ApJ*, 563, 118
- Poggianti, B. M. 2003, *Ap&SS*, 285, 121
- Poggianti, B. M., Bridges, T. J., Komiyama, Y., Yagi, M., Carter, D., Mobasher, B., Okamura, S., & Kashikawa, N. 2004, *ApJ*, 601, 197
- Rakos, K., Dominis, D., Steindling, S., 2001, *A&A*, 369
- Rix, H., Barden, M., Beckwith S.V.W., et al., 2006, *ApJS*, 152, 163
- Roth, M.M., Kelz, A., Fechner, T., et al., 2005, *PASP*, 117, 620
- Salpeter, E. E. 1955, *ApJ*, 121, 161
- Sánchez, S. F., & González-Serrano, J. I. 2002, *A&A*, 396, 773
- Sánchez S.F., 2004, *AN*, 325, 167
- Sánchez S.F., García-Lorenzo, B., Mediavilla, E., et al., 2004, *ApJ*, 615, 156
- Sánchez, S. F., et al. 2004, *ApJ*, 614, 586
- Sánchez S.F. & N.Cardiell, *Calar Alto Newsletter*, num. 10
- Sánchez S.F., 2006, *AN*, 327, 850
- Sánchez, S. F., García-Lorenzo, B., Jahnke, K., Mediavilla, E., González-Serrano, J. I., Christensen, L., & Wisotzki, L. 2006, *New Astronomy Review*, 49, 501
- Sánchez S.F., García-Lorenzo, B., Mediavilla, E., 2006, *Proceedings of the XIII IAC Winter School*, Arribas, S., Mediavilla, E., & Roth, M., Ed., in press.
- Sérsic, J. L. 1968, *Atlas de Galaxias Australes* (Córdoba, Argentina: Press of the Universidad Nacional)
- Simien, F., & de Vaucouleurs, G. 1986, *ApJ*, 302, 564
- Sirianni, M., et al. 2005, *PASP*, 117, 1049
- Smail, I., Dressler, A., Couch, W. J., Ellis, R. S., Oemler, A. J., Butcher, H., & Sharples, R. M. 1997, *ApJS*, 110, 213
- Smail, I., Edge, A. C., Ellis, R. S., & Blandford, R. D. 1998, *MNRAS*, 293, 124
- Smail, I., Kuntschner, H., Kodama, T., et al. 2001, *MNRAS*, 323, 839
- Stanford et al. 1997, *AJ*, 114, 2232
- Stanford et al. 1998, *ApJ*, 492, 461
- Thomas, D., Greggio, L., & Bender, R. 1999, *MNRAS*, 302, 537
- Thomas D., Maraston C., Korn A., 2004, *MNRAS*, 351, L19
- Thompson, L. A. 1986, *ApJ*, 300, 639
- Thompson, L. A. 1988, *ApJ*, 324, 112
- Tinsley B., 1980, *Fund. Cosmic Physics*, 5, 287
- Tody, D. 1993, "IRAF in the Nineties" in *Astronomical Data Analysis Software and Systems II*, A.S.P. Conference Ser., Vol 52, eds. R.J. Hanisch, R.J.V. Brissenden, & J. Barnes, 173.
- Trager, S. C., Worthey, G., Faber, S. M., Burstein, D., & Gonzalez, J. J. 1998, *ApJS*, 116, 1
- Trager, S. C., Faber, S. M., Worthey, G., & Gonzalez, J. J. 2000, *AJ*, 120, 165
- Thuan, T. X., & Gunn, J. E. 1976, *PASP*, 88, 543
- Vazdekis A., Cenarro A.J., Gorgas J., Cardiel N., Peletier R.F., 2003, *MNRAS*, 340, 1317
- van Dokkum & Franx 1996, *MNRAS*, 281, 985
- van Dokkum, P. G., Franx, M., Fabricant, D., Kelson, D. D., & Illingworth, G. D. 1999, *ApJL*, 520, L95
- van Dokkum et al. 2001b., *ApJ*, 553, 90
- Verheijen, M. A. W. 1997, Ph.D. Thesis,
- Verheijen, M. A. W., Bershady, M. A., Andersen, D. R., Swaters, R. A., Westfall, K., Kelz, A., & Roth, M. M. 2004, *Astronomische Nachrichten*, 325, 151
- Wolf, C., et al. 2005, *ApJ*, 630, 771
- Worthey G., 1994, *ApJS*, 95, 107
- Worthey G., 1994, *ApJS*, 111, 377
- Worthey G, Faber S.M., González J.J., Burstein D., 1994, *ApJS*, 94, 687
- Zwaan, M. A., van Dokkum, P. G., & Verheijen, M. A. W. 2001, *Science*, 293, 1800
- Ziegler, B.L., Bower, R.G., Smail, I., et al., 2001, *MNRAS*, 325, 1571

APPENDIX A: INDIVIDUAL SPECTRUM

Figure A1 shows the individual spectrum extracted from our IFS data for each galaxy listed in the Table 4. For each galaxy the spectrum is plotted together with the multi-band broad-band photometry derived from the HST/ACS F475W, F555W, F625W, F775W and F850LP-band images (red circles). The vertical error bars indicate the photometric errors, while the horizontal ones indicate the width of each band. The wavelength of the strongest night sky emission lines and bands are also indicated. At these locations the improper sky subtraction produces characteristic residuals that can be seen in the spectra. In particular the wavelength range redder than 7200Å is strongly affected, so we did not consider it in any of the performed analysis. The grey solid line shows the best fitted SSP model derived with the procedure described in Section 3.7.2.

APPENDIX B: MORPHOLOGICAL ANALYSIS AND SPECTRA EXTRACTION: CHROMATIC EFFECTS

The procedure to deblend and extract the spectra of the individual objects from our IFS data relies on the assumption that it is possible to use the morphological parameters derived by fitting galaxy profile models on the F850LP-band image, using `galfit`, to derive the photometry at any other wavelength range, by forcing `galfit` to recover the flux with the morphological parameters fixed. To test this assumption we use the HST/ACS multiband image dataset, which cover all the wavelength range of our IFS data.

For each broad-band image of our dataset (F475W, F555W, F625W and F775W), we performed the same morphological analysis that we already performed for the F850LP-band, following the prescriptions described in Section 3.2. In this first iteration we left `galfit` to fit the morphological parameters, as we did in the analysis of the F850LP-band. This procedure produces a morphological catalogue for each of the considered images, including the same parameters listed in Table 3. In a second iteration, the analysis was repeated but this time we used as input parameters the ones derived by the analysis of the F850LP-band image. In this second step the morphological parameters were fixed to those input values, and only the photometry was fitted by `galfit`. This procedure is basically the same that we use to extract and deblend the spectra in our IFS data.

Similar results have been found for any band. Figure B1 summarizes the results from the analysis. Left-panel shows a comparison between the different bands magnitudes derived by `galfit` forcing the morphological parameters to be the ones derived from the morphological analysis of the F850LP-band image, and the magnitudes derived not imposing any condition to `galfit` regarding the morphological parameters of the analyzed objects. The magnitudes derived using both methods agree within ± 0.2 mags, without any clear trend or bias. Middle-panel shows the scale-length derived by `galfit` for the F850LP-band image, using in the forced fitting process over the different bands' images described above, along the scale-length derived directly over this image by the morphological analysis. Although there are some outliers, both scale-lengths are similar in most of the cases. Right-panels shows a similar comparison between the Sérsic indices derived by the two fitting procedures. In this last case we found the biggest differences between both parameters, with a considerable dispersion from the one-to-one relation. It is clear that there is a chromatic effect over the morphology, as it is seen in the last panel, however, this effect has a reduced impact on the derived scale-length, and even less impact on the derived photometry. Thus, the basic assumption of our procedure to deblend and extract the individual spectra of the targets from our IFS data is valid.

To perform a final test of the validity of our procedure and the accuracy of our spectrophotometric data we synthesized the fluxes throughout the *B*, *V*, *R* and *I*-bands for each of our 28 cluster members with IFS data by convolving their extracted spectra with the corresponding HST/ACS filter band transmission curve, integrating their fluxes. These fluxes are compared to the corresponding ones derived using the HST/ACS based photometry listed in Table 2. Figure B2 shows the histograms of the relative differ-

ences between both fluxes for each band, $\Delta F/F$, that basically corresponds to the error in the corresponding magnitude ($\sim e_{mag}$). Due to the high accuracy of the HST/ACS photometry (typical $e_{mag} \sim 0.05$ mag for the considered objects) most of the differences shown in the figure corresponds to spectrophotometric errors in the IFS data. For all the bands both fluxes agree within a range of ± 0.3 mag, with a standard deviation of the difference of ~ 0.15 mag.

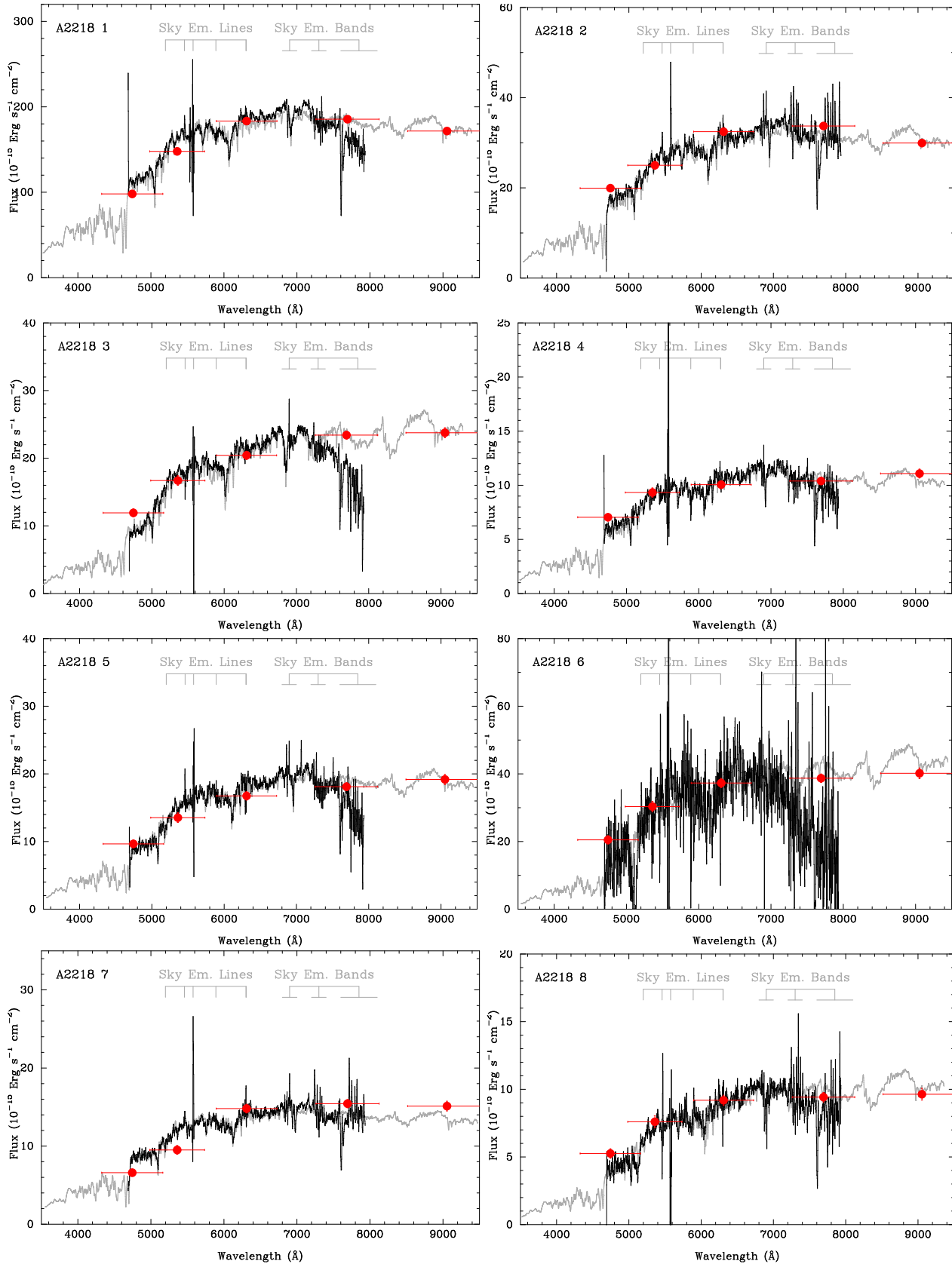


Figure A1. Individual extracted spectrum for each of the confirmed cluster members within the field-of-view of our IFS data (black solid line), each one labeled with the identification number listed in Table 4. For each galaxy the spectrum is plot together with the multiband broad-band photometry derived from the HST/ACS F475W, F555W, F625W, F775W and F850LP-band images (red circles). The vertical error bars indicate the photometric errors, while the horizontal ones indicate the width of each band. The grey solid line shows the best fitted SSP model derived with the procedure described in Section 3.7.2.

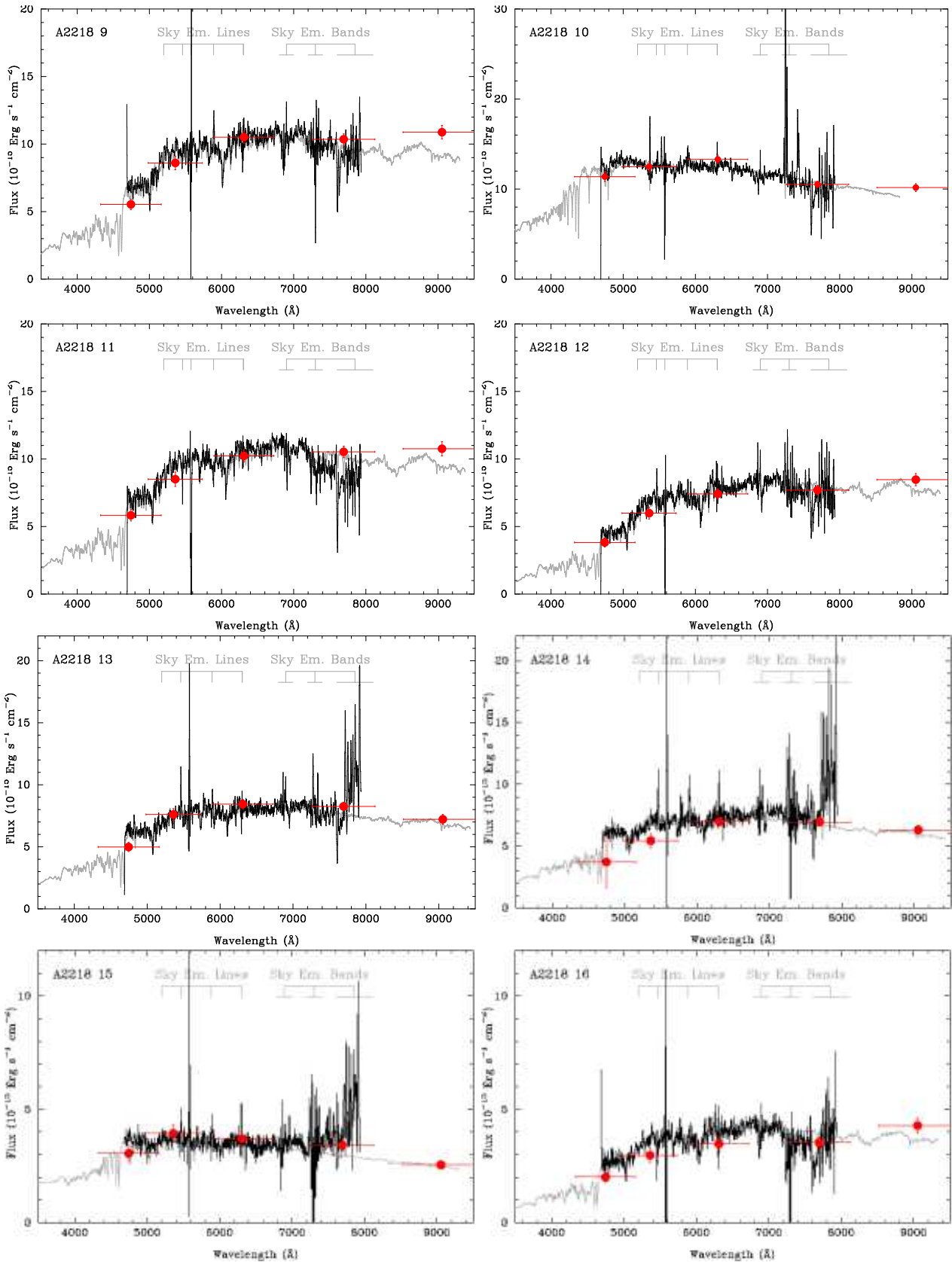


Figure A2. Continue

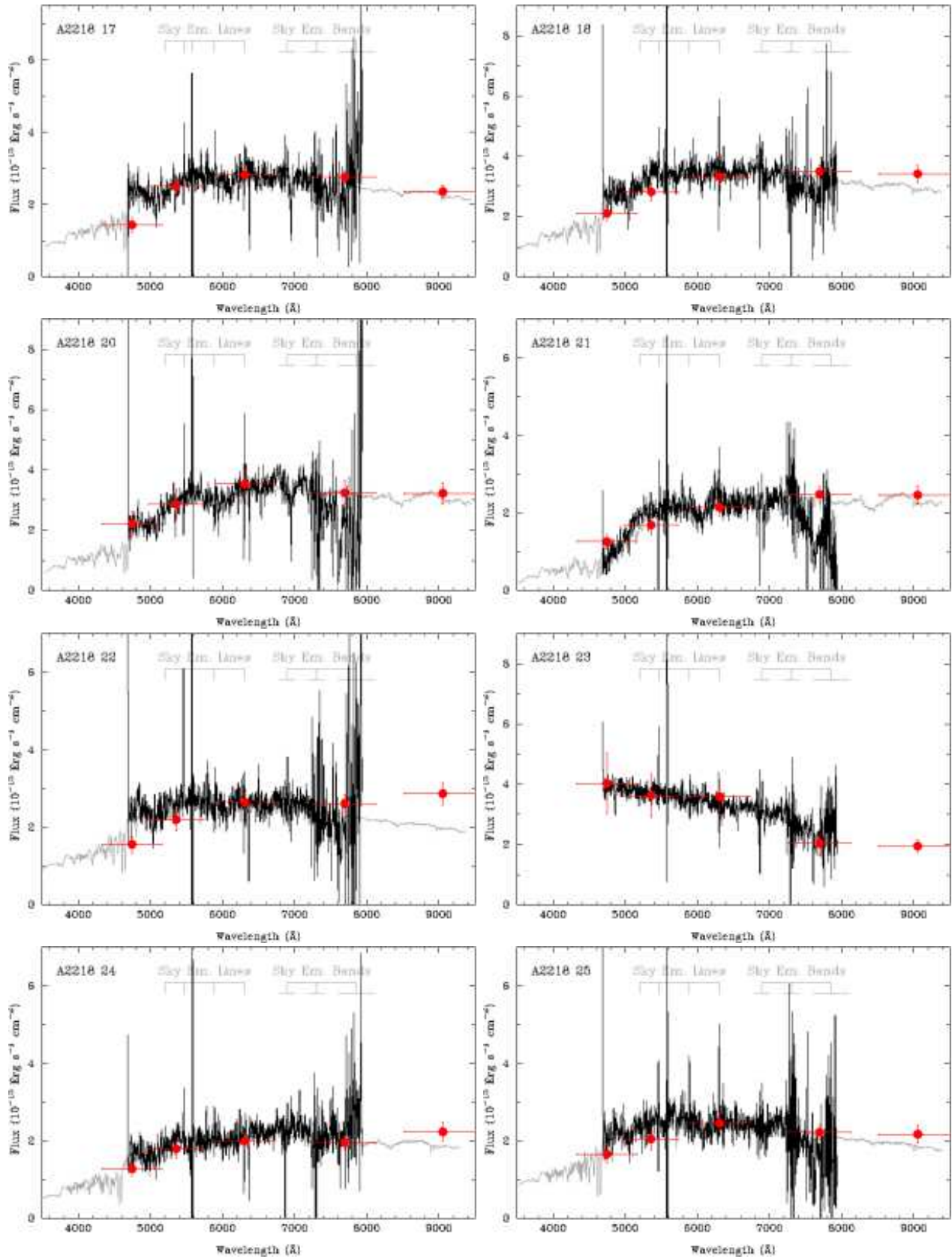


Figure A3. Continue

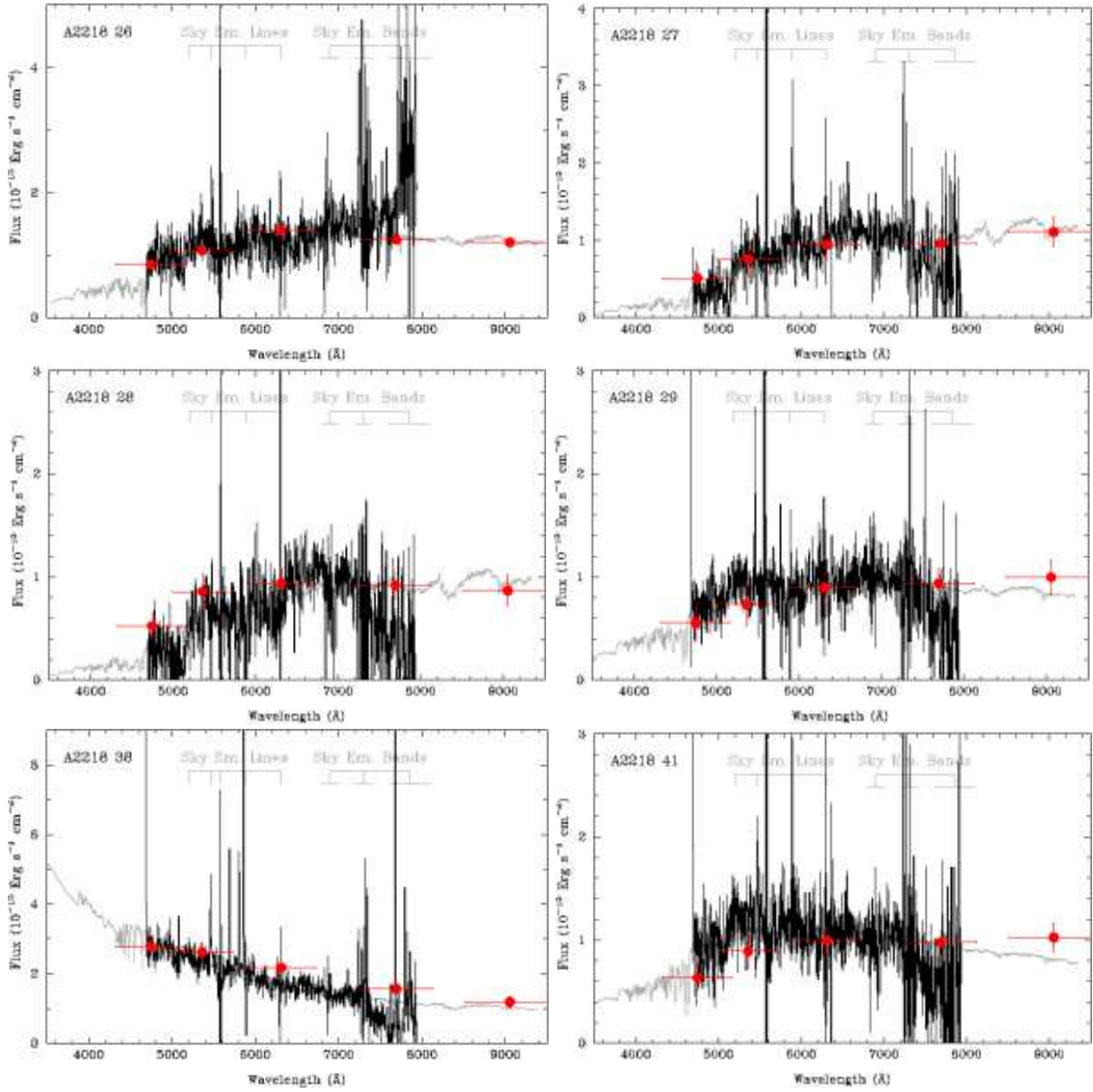


Figure A4. Continue

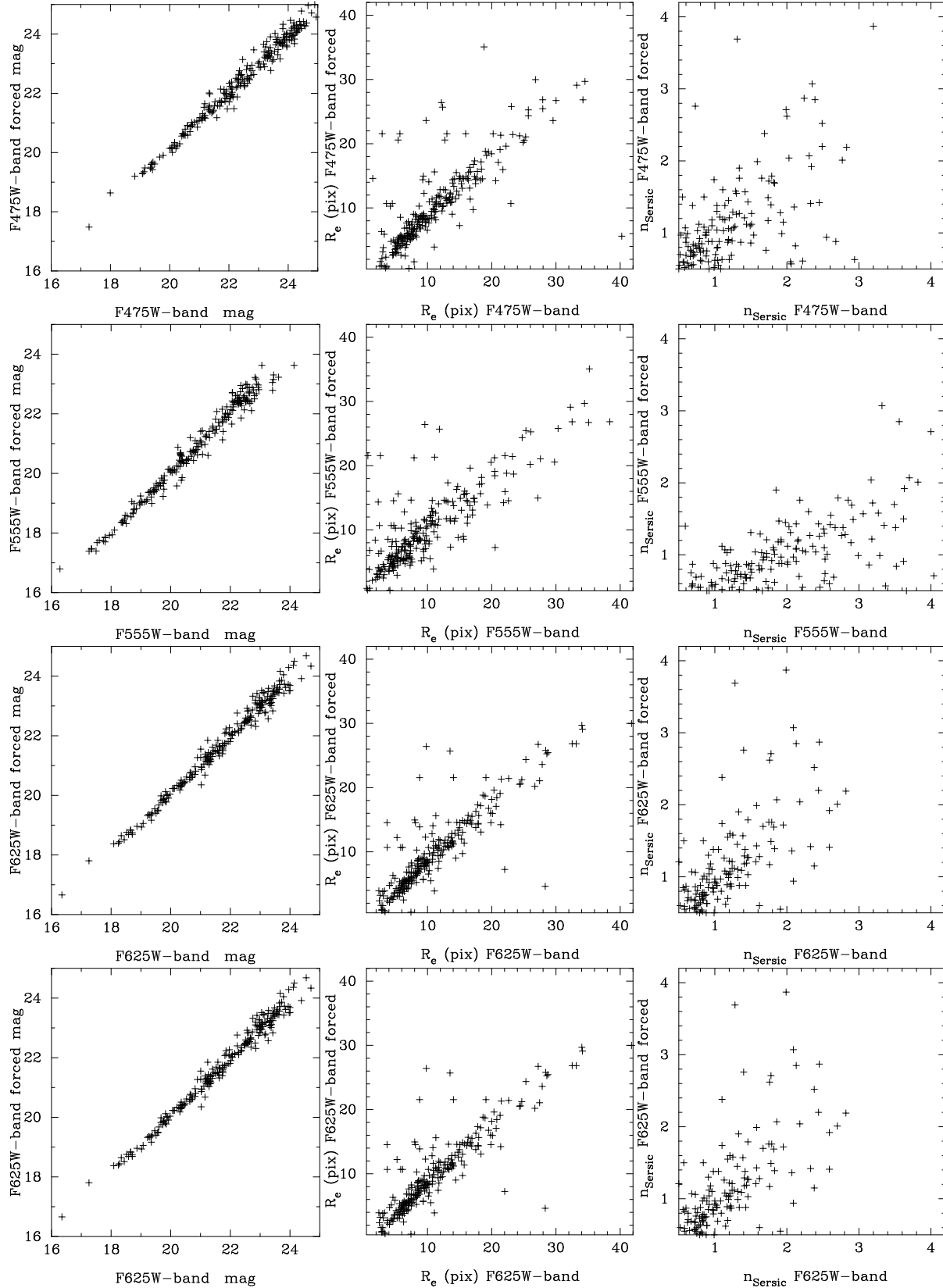


Figure B1. *left-panels:* F475W, F555W, F625W and F775W-band magnitudes derived by *galfit* forcing the morphological parameters to be the ones derived from the morphological analysis of the F850LP-band image, as a function of the same magnitudes derived not imposing any condition to *galfit* regarding the morphological parameters of the analyzed objects. *middle-panels:* similar comparison for the length-scales derived by *galfit* for the F850LP-band image and for any other band. *right-panels:* similar comparison for the Sérsic indices.

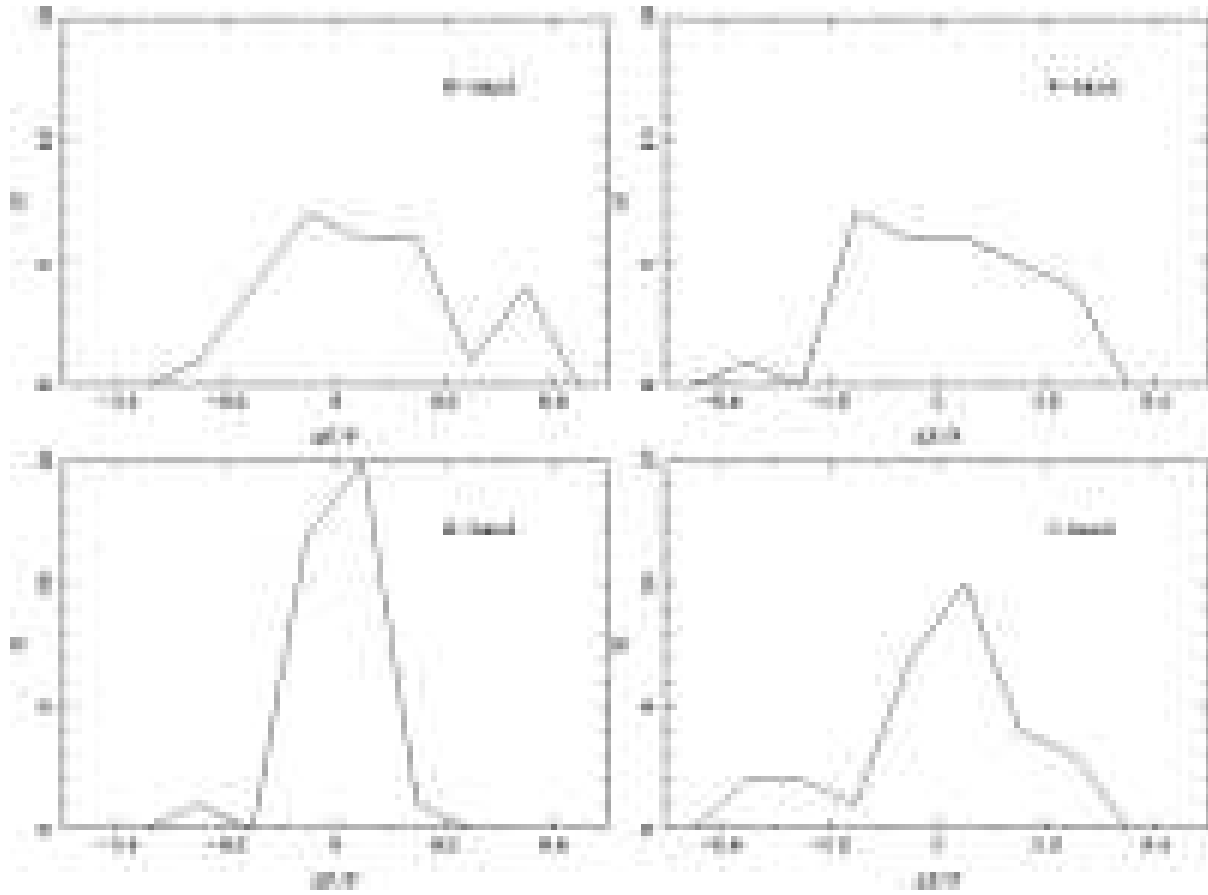


Figure B2. Relative differences between the fluxes obtained for the B, V, R and I -bands derived from the IFS extracted spectra and those ones derived using the photometry obtained from the HST/ACS images.

